# Phase-field method based on discrete unified gas-kinetic scheme for large-density-ratio two-phase flows

Zeren Yang (杨泽人),[*] Chengwen Zhong (钟诚文),[†] and Congshan Zhuo (卓丛山)[‡]
*National Key Laboratory of Science and Technology on Aerodynamic Design and Research, Northwestern Polytechnical University, Xi'an, Shaanxi 710072, China*

(Received 10 October 2018; published 3 April 2019)

In this paper, a phase-field method under the framework of discrete unified gas-kinetic scheme (DUGKS) for incompressible multiphase fluid flows is proposed. Two kinetic models are constructed to solve the conservative Allen-Cahn equation that accounts for the interface behavior and the incompressible hydrodynamic equations that govern the flow field, respectively. With a truncated equilibrium distribution function as well as a temporal derivative added to the source term, the macroscopic governing equations can be exactly recovered from the kinetic models through the Chapman-Enskog analysis. Calculation of source terms involving high-order derivatives existed in the quasi-incompressible model is simplified. A series of benchmark cases including four interface-capturing tests and four binary flow tests are carried out. Results compared to that of the lattice Boltzmann method (LBM) have been obtained. A convergence rate of second order can be guaranteed in the test of interface diagonal translation. The capability of the present method to track the interface that undergoes a severe deformation has been verified. Stationary bubble and spinodal decomposition problems, both with a density ratio as high as 1000, are conducted and reliable solutions have been provided. The layered Poiseuille flow with a large viscosity ratio is simulated and numerical results agree well with the analytical solutions. Variation of positions of the bubble front and spike tip during the evolution of Rayleigh-Taylor instability has been predicted precisely. However, the detailed depiction of complicated interface patterns appearing during the evolution process is failed, which is mainly caused by the relatively large numerical dissipation of DUGKS compared to that of LBM. A high-order DUGKS is needed to overcome this problem.

DOI: 10.1103/PhysRevE.99.043302

## I. INTRODUCTION

Numerical simulation of multiphase fluid flows has drawn the attention of many researchers for decades due to its importance in scientific and engineering applications. With the rapid progress in computational technology, various numerical methods including the volume of fluid (VOF) method [1], level set approach [2], front tracking method [3], diffuse interface method [4,5], and smoothed particle hydrodynamics method [6,7] have been developed. Among those methods, the diffuse interface model has shown great advantage by virtue of its energy-based variational formalism as well as its simplification in the description of interface evolution. Many of the kinetic schemes [8–11], aiming at modeling phase behaviors at the mesoscopic level and bridging the gap between the macroscopic features and microscopic intermolecular interactions in multiphase systems, can be categorized into the diffuse interface method.

As one of many popular kinetic schemes, the lattice Boltzmann (LB) method has received great attention due to its simplicity in the application of intermolecular interactions. In the framework of the LB method, mainly four kinds of multiphase models, including color-gradient model [12], pseudopotential model [13,14], free-energy model [15,16], and phase-field based model [16,17], are proposed based on different physical pictures. These LB models have been improved continuously by plenty of research since the moment they were born and significant progresses on their performance have been made [18–23]. While they share the same advantages of the LB method, such as simplicity and efficiency, relatively low dissipation, and intrinsic kinetic nature [24], they are also limited by the drawbacks of the LB method, one of which is the required uniformity of the lattice structure imposed by the symmetry of the predefined lattice velocities. In order to capture the interface precisely and efficiently, either a high resolution scheme or adaptive mesh refinement (AMR) technique is usually employed in the simulation of multiphase problems. The usage of uniform mesh is surely a waste of time and computational resources. However, application of the AMR technique to the LB method would result in a loss of its simplicity. The multiphase lattice Boltzmann flux solver (MLBFS) aims to combine the advantages of Navier-Stokes solvers and LB method in the simulation of multiphase flows, which was first proposed by Wang *et al.* [10,25]. In their work, a fifth-order upwind scheme is adopted to solve the Cahn-Hilliard (CH) equation that governs the evolution of interface and a lattice Boltzmann flux scheme is used to evaluate the flux at cell interface for the mass and momentum equation. A density ratio of 1000 with Reynolds number up to 3000

[*]zeren@mail.nwpu.edu.cn
[†]Corresponding author: zhongcw@nwpu.edu.cn
[‡]zhuocs@nwpu.edu.cn

 ©2019 American Physical Society

is achieved in the simulation of Rayleigh-Taylor instability (RTI). Pan *et al.* [11] developed a two-stage fourth-order gas-kinetic scheme (GKS) for the simulation of compressible multicomponent flows. Based on a simplified two-species BGK model, a set of coupled Euler equations that accounts for different components are constructed and solved by a fourth-order gas-kinetic scheme. Various numerical tests, including shock-bubble interaction, Rayleigh-Taylor instability, etc., have verified the reliability of this approach. MLBFS and GKS show a common philosophy in the construction of flux since kinetic schemes, although different in detail, are introduced for both methods, which is also the only point where they have a relationship with kinetic schemes. Furthermore, both of these two methods lack the ability of depicting the nonequilibrium effects in the flow field. Gan *et al.* [9] proposed a discrete Boltzmann model (DBM) to study the process of phase separation based on the work of Gonnella *et al.* [26]. The interplay between interparticle forces that drives changes and gradient force that opposes them is simulated and the nonequilibrium effects behind the phenomenon are investigated thoroughly, which provides a better understanding of the nonequilibrium behaviors underneath the phase separation process. Later, the DBM is applied to the simulation of Rayleigh-Taylor instability in compressible flows [27,28]. The relations between effects of compressibility and global nonequilibrium intensity are investigated and a negative correlation is observed. The DBM provides a distinctive way for the explanation of a physical phenomenon from a viewpoint of nonequilibrium effects. However, it suffers from the time step restriction by collision time, which imposes a negative impact on its efficiency.

The discrete unified gas-kinetic scheme (DUGKS) proposed by Guo *et al.* [29,30] is a new type of kinetic scheme which combines the advantages of both the LB method in its discrete conservative collision operator and gas-kinetic scheme in its flux modeling [31]. As a finite volume method, it overcomes the disadvantage of uniform mesh with which the LB method has to comply and simplifies the calculating routine in the evaluation of flux at the cell interface. The fully coupling of streaming and collision processes in DUGKS ensures a low numerical dissipation feature. The semi-implicit treatment of the collision term in DUGKS also makes an improvement in its numerical stability [32]. Furthermore, the evolution equation rather than direct interpolation is employed in the evaluation of flux, which contributes to its asymptotic preserving (AP) feature [30]. That means the time step in only limited by the Courant-Friedrichs-Lewy (CFL) condition rather than the collision time in the framework of DUGKS. Compared to the other discrete velocity methods, DUGKS has shown a better performance in terms of modeling accuracy and computational efficiency when the hydrodynamic flow regime is dominant [33]. Due to its various advantages, DUGKS has been applied to modeling force driven flows [34], nonequilibrium flows [35,36], phonon transportation [37], binary gas mixtures [38], and fluid-particle flows [39,40]. Recently, Zhang *et al.* [41] extend the DUGKS to two-phase flows based on a quasi-incompressible phase-field governing equation. The accuracy and stability of this method have been verified. However, the density contrast of different phases in their work is relatively low and no interface capturing test is given to evaluate the capability of DUGKS under such a circumstance. To make a further extension of DUGKS on the simulation of two-phase problems, we proposed a method by applying DUGKS to the solution of the conservative Allen-Cahn (AC) equation [42–44]. The incompressible hydrodynamic equations from Liang *et al.* [23] are also implemented in the DUGKS framework. Various interface capturing tests are conducted and binary flow cases with a high density ratio are studied.

The rest of this article is organized as follows. In Sec. II, the methodology of the proposed model for two-phase flows will be introduced. In Sec. III, several benchmark tests are conducted to validate the capability of the current method to capture the interface in two-phase flows. In Sec. IV, typical two-phase flow cases are carried out to study the performance of our model. A brief summary is drawn in Sec. V.

## II. METHODOLOGY

### A. Governing equation for two-phase flows

Based on the phase-field theory, a Helmholtz free energy functional dependent upon an order parameter $\phi$ is used to describe the thermodynamic behavior of a two-phase fluid system [45]

$$F(\phi) = \int_V \left( \epsilon(\phi) + \frac{\kappa}{2} |\nabla \phi|^2 \right) dV, \tag{1}$$

where $V$ is the domain of the system, and $\epsilon(\phi)$ refers to the bulk energy density. For binary fluid system, the function of bulk energy density usually has the following double-well form:

$$\epsilon(\phi) = \beta(\phi - \phi_H)^2(\phi - \phi_L)^2, \tag{2}$$

which has two minima corresponding to the two phases of the fluid. The parameters $\beta$ and $\kappa$ are two positive constants determined by both the surface tension coefficient $\sigma$ and the width of interface $W$:

$$\kappa = \frac{3}{2}\sigma W, \quad \beta = \frac{12\sigma}{W}. \tag{3}$$

The chemical potential $\mu_\phi$ is defined as the variation of the free energy with respect to the order parameter

$$\begin{aligned} \mu_\phi &= \frac{\delta F(\phi)}{\delta \phi} \\ &= 4\beta(\phi - \phi_H)(\phi - \phi_L)\left( \phi - \frac{\phi_H + \phi_L}{2} \right) - \kappa \Delta \phi. \end{aligned} \tag{4}$$

The equation used for interface tracking in this study is the following conservative Allen-Cahn equation [44]:

$$\frac{\partial \phi}{\partial t} + \nabla \cdot (\phi \boldsymbol{u}) = \nabla \cdot [\mathrm{M}_\phi (\nabla \phi - \theta \boldsymbol{n})], \tag{5}$$

where $t$ is the time, $\boldsymbol{u}$ is the transportation velocity, $\mathrm{M}_\phi$ is the mobility coefficient, and $\boldsymbol{n}$ is the local unit vector normal to the interface. $\theta$ is interpreted as a function of $\phi$:

$$\theta = \frac{-4(\phi - \phi_H)(\phi - \phi_L)}{W(\phi_H - \phi_L)}. \tag{6}$$

The equilibrium profile of $\phi$ along the direction normal to the interface assumes a hyperbolic tangent form

$$\phi(z) = \frac{\phi_H + \phi_L}{2} + \frac{\phi_H - \phi_L}{2}\tanh\left(\frac{2z}{W}\right), \tag{7}$$

where $z$ is the coordinate along interface normal. The location of actual interface is determined by $\phi = 0.5(\phi_H + \phi_L)$, where $\phi_H = 1$ denotes the heavy fluid and $\phi_L = 0$ indicates the light fluid.

For an exhaustive derivation of the conservative AC equation, one is recommended to refer to Ren *et al.* [46]. It is worth noting that divergence-free velocity condition was introduced during this derivation.

The hydrodynamic equations used for a two-phase fluid system are chosen to be

$$\nabla \cdot \boldsymbol{u} = 0, \tag{8}$$

$$\frac{\partial(\rho \boldsymbol{u})}{\partial t} + \nabla \cdot (\rho \boldsymbol{u}\boldsymbol{u}) = -\nabla p + \nabla \cdot [\mu(\nabla \boldsymbol{u} + \nabla \boldsymbol{u}^T)] + \boldsymbol{F}, \tag{9}$$

where $\boldsymbol{F}$ consists of the surface tension force $\boldsymbol{F}_s = \mu_\phi \nabla \phi$ and the gravitational force $\boldsymbol{G}$, if present. The relationship between order parameter $\phi$ and density $\rho$ is

$$\rho = \frac{\rho_H - \rho_L}{\phi_H - \phi_L}(\phi - \phi_L) + \rho_L. \tag{10}$$

Substituting Eqs. (5) and (8) into (10), we can get the nonconservative mass equation

$$\frac{\partial \rho}{\partial t} + \nabla \cdot (\rho \boldsymbol{u}) = \frac{\rho_H - \rho_L}{\phi_H - \phi_L}\nabla \cdot [\mathrm{M}_\phi(\nabla \phi - \theta \boldsymbol{n})]. \tag{11}$$

The point we are trying to clarify here is that with the divergence-free velocity condition, the uniform conservative mass equation cannot be derived from the conservative Allen-Cahn equation. The conservativeness of mass equation can be guaranteed only if the density gradient equals zero, which means that mass generation or consumption exists during the process of phase transition when density contrast exists. As is depicted by Li *et al.* [47], the uniform mass conservation and the incompressibility condition cannot be satisfied at the same time because of the volume diffusive flux across the interfacial region. Hence, it is not the mass parameter $\rho$ but the order parameter $\phi$ that conservativeness qualifies. To eliminate the nonconservative property of mass, either the quasi-incompressible model [48] or the nonlocal AC equation [49] can be used.

### B. DUGKS for two-phase equations

The discrete kinetic equations used to interpret phase equation (5) and hydrodynamic equation (9) are

$$\frac{\partial f_i}{\partial t} + \xi_i \cdot \nabla f_i = -\frac{f_i - f_i^{eq}}{\tau_f} + S_i^f, \tag{12}$$

$$\frac{\partial g_i}{\partial t} + \xi_i \cdot \nabla g_i = -\frac{g_i - g_i^{eq}}{\tau_g} + S_i^g, \tag{13}$$

where $f_i$ and $g_i$, corresponding to the phase order $\phi$ and density $\rho$, are the particle distribution functions in terms of position $\boldsymbol{x}$, discrete particle velocity $\boldsymbol{\xi}_i$, and time $t$. $\tau_f$ and $\tau_g$ are the relaxation times related to the mobility coefficient and dynamic viscosity, respectively. $f_i^{eq}$ and $g_i^{eq}$ are the equilibrium distribution functions with specific forms. $S_i^f$ and $S_i^g$ are the source terms.

The three-point Gauss-Hermite quadrature is employed in this work to get the discrete particle velocities in one dimension. The discrete velocities and associated weights in two dimensions can be achieved by the tensor product method

$$\boldsymbol{\xi} = \sqrt{3RT}\begin{bmatrix} 0 & 1 & 1 & 0 & -1 & -1 & -1 & 0 & 1 \\ 0 & 0 & 1 & 1 & 1 & 0 & -1 & -1 & -1 \end{bmatrix},$$

$$\omega_i = \begin{cases} \frac{4}{9}, & i = 0 \\ \frac{1}{9}, & i = 1, 3, 5, 7 \\ \frac{1}{36}, & i = 2, 4, 6, 8. \end{cases} \tag{14}$$

The equilibrium distribution function for $f_i^{eq}$ is expressed as

$$f_i^{eq} = \omega_i \phi\left(1 + \boldsymbol{\xi_i} \cdot \boldsymbol{u}/c_s^2\right), \tag{15}$$

where $c_s = \sqrt{RT}$ is the sound speed. Ren *et al.* [46] and Wang *et al.* [50] both pointed out that by discarding high-order terms of velocity, an exact form of AC equation achieved through Chapman-Enskog (CE) analysis can be guaranteed. The source term $S_i^f$ consists of two parts and is defined as

$$S_i^f = \omega_i \theta \boldsymbol{\xi_i} \cdot \boldsymbol{n} + \omega_i \boldsymbol{\xi_i} \partial_t(\phi \boldsymbol{u})/RT. \tag{16}$$

The second part is necessary to eliminate the term of $\partial_t(\phi \boldsymbol{u})$ introduced via the CE expansion.

The equilibrium distribution function for $g_i^{eq}$ is [23,51]

$$g_i^{eq} = \begin{cases} \frac{p}{RT}(\omega_i - 1) + \rho(\Gamma_i(\boldsymbol{u}) - \Gamma_i(0)), & i = 0 \\ \frac{p}{RT}\omega_i + \rho[\Gamma_i(\boldsymbol{u}) - \Gamma_i(0)], & i \neq 0 \end{cases} \tag{17}$$

where

$$\Gamma_i(\boldsymbol{u}) = \omega_i\left[1 + \frac{\boldsymbol{\xi}_i \cdot \boldsymbol{u}}{RT} + \frac{(\boldsymbol{\xi}_i \cdot \boldsymbol{u})^2}{2(RT)^2} - \frac{\boldsymbol{u} \cdot \boldsymbol{u}}{2RT}\right]. \tag{18}$$

The source term $S_i^g$ is defined as

$$S_i^g = \frac{(\boldsymbol{\xi}_i - \boldsymbol{u})}{RT} \cdot \{[\Gamma_i(\boldsymbol{u}) - \Gamma_i(0)]\nabla(\rho RT) + (\boldsymbol{F}_s + \boldsymbol{G})\Gamma_i(\boldsymbol{u})\}. \tag{19}$$

It needs to be mentioned that Liang *et al.* [52] proposed a simplified force model by discarding the term of $O(\delta_t Ma^2)$ during the CE analysis, which works well when the magnitude of flow velocity is relatively small. To keep rigorous and general property of the present scheme, however, the force model previously used by Liang *et al.* [23] is applied. By choosing the appropriate expression for equilibrium distribution functions and source terms, we can get the exact hydrodynamic equations from the discrete kinetic equations via the CE analysis, details of which are shown in the Appendix.

Since Eqs. (12) and (13) share the same format, a new symbol $\psi$ is introduced to substitute either $f$ or $g$ for the convenience of illustration. Thus, the unified form of discrete kinetic equation is

$$\frac{\partial \psi_i}{\partial t} + \xi_i \cdot \nabla \psi_i = -\frac{\psi_i - \psi_i^{eq}}{\tau_f} + S_i^\psi. \tag{20}$$

The DUGKS is applied to solve the above equation for its various advantages [32,53]. Integrating it over a control volume $V_j$ centered at $\boldsymbol{x}_j$ from time $t_n$ to $t_{n+1}$, we get

$$\psi_i^{n+1} - \psi_i^n + \frac{\Delta t}{|V_j|} J^{\psi,n+1/2} = \frac{\Delta t}{2}\left[\Omega_i^{\psi,n+1} + \Omega_i^{\psi,n}\right] + \frac{\Delta t}{2}\left[S_i^{\psi,n+1} + S_i^{\psi,n}\right], \quad (21)$$

where $\Omega_i^{\psi} = -(\psi_i - \psi_i^{eq})/\tau_{\psi}$, $V_j$ is the volume of cell with index $j$, $n$ is the time. $J^{\psi,n+1/2}$ is the microflux across the cell interface at the middle of current time interval with the following form:

$$\boldsymbol{J}^{\psi,n+1/2} = \int_{\partial V_j} (\boldsymbol{\xi}_i \cdot \boldsymbol{n})\psi_i(\boldsymbol{x}_f, \boldsymbol{\xi}_i, t_{n+1/2}) d\boldsymbol{S}, \quad (22)$$

where $\partial V_j$ is the surface of cell $V_j$, $\boldsymbol{n}$ is the outward unit vector normal to the surface element $dS$, and $\boldsymbol{x}_f$ denotes the position of surface element. Trapezoidal rule is employed for the integration of the collision term $\Omega_i^{\psi}$ and source term $S_i^{\psi}$, and midpoint rule is chosen for the evaluation of the microflux $J^{\psi,n+1/2}$. To overcome the implicit treatment of source terms in Eq. (21), two auxiliary distribution functions are introduced [29,30]:

$$\tilde{\psi}_i = \psi_i - \frac{\Delta t}{2}\Omega_i - \frac{\Delta t}{2}S_i = \frac{2\tau_{\psi} + \Delta t}{2\tau_{\psi}}\psi_i - \frac{\Delta t}{2\tau_{\psi}}\psi_i^{eq} - \frac{\Delta t}{2}S_i, \quad (23a)$$

$$\tilde{\psi}_i^{+} = \psi_i + \frac{\Delta t}{2}\Omega_i + \frac{\Delta t}{2}S_i = \frac{2\tau_{\psi} - \Delta t}{2\tau_{\psi}}\psi_i + \frac{\Delta t}{2\tau_{\psi}}\psi_i^{eq} + \frac{\Delta t}{2}S_i. \quad (23b)$$

Substituting Eq. (23) into (21) and rearranging each of these terms according to the time step, we have

$$\tilde{\psi}_i^{n+1} = \tilde{\psi}_i^{+,n} - \frac{\Delta t}{|V_j|}\boldsymbol{J}^{\psi,n+1/2}. \quad (24)$$

Instead of the original distribution function $\psi$, the auxiliary distribution function $\tilde{\psi}$ is updated. The key step to obtain an accurate $\tilde{\psi}$ lies in the evaluation of flux $J^{\psi,n+1/2}$. To get the original distribution function at intermediate moment of a time interval, Eq. (20) is integrated along its characteristic line within a half time step $h = \Delta t/2$:

$$\psi_i(\boldsymbol{x}_f, t_n + h) - \psi_i(\boldsymbol{x}_f - \boldsymbol{\xi}_i h, t_n) = \frac{h}{2}\left[\Omega_i^{\psi}(\boldsymbol{x}_f, t_n + h) + \Omega_i^{\psi}(\boldsymbol{x}_f - \boldsymbol{\xi}_i h, t_n)\right] + \frac{h}{2}\left[S_i^{\psi}(\boldsymbol{x}_f, t_n + h) + S_i^{\psi}(\boldsymbol{x}_f - \boldsymbol{\xi}_i h, t_n)\right]. \quad (25)$$

Again, to remove the implicit treatment of the collision term and source term, two auxiliary distribution functions are introduced:

$$\bar{\psi}_i = \psi_i - \frac{h}{2}\Omega_i^{\psi} - \frac{h}{2}S_i^{\psi} = \frac{2\tau_{\psi} + h}{2\tau_{\psi}}\psi_i - \frac{h}{2\tau_{\psi}}\psi_i^{eq} - \frac{h}{2}S_i^{\psi}, \quad (26a)$$

$$\bar{\psi}_i^{+} = \psi_i + \frac{h}{2}\Omega_i^{\psi} + \frac{h}{2}S_i^{\psi} = \frac{2\tau_{\psi} - h}{2\tau_{\psi}}\psi_i + \frac{h}{2\tau_{\psi}}\psi_i^{eq} + \frac{h}{2}S_i^{\psi}. \quad (26b)$$

As a result, Eq. (25) turns into

$$\bar{\psi}_i(\boldsymbol{x}_f, t_n + h) = \bar{\psi}_i^{+}(\boldsymbol{x}_f - \boldsymbol{\xi}_i h, t_n), \quad (27)$$

which is the most ingenious step in the evaluation of flux. An indispensable particle distribution function $\bar{\psi}_i(\boldsymbol{x}_f, t_n + h)$ that is related with the next half time step is reconstructed by tracing this set of particles back to the current time step, with the collision and force effects taken into consideration.

Two approaches, central scheme and upwind scheme, were put forward by Guo *et al.* [29,30] successively to obtain the value of $\bar{\psi}_i^{+}(\boldsymbol{x}_f - \boldsymbol{\xi}_i h, t_n)$. Since the simulation of two-phase flow demands a low numerical dissipation on the algorithm, the central scheme is used in this study. After the update of auxiliary distribution function $\bar{\psi}_i(\boldsymbol{x}_f, t_n + h)$ and macroscopic variables located at the cell interface, the original distribution function can be calculated by

$$\psi_i = \frac{2\tau_{\psi}}{2\tau_{\psi} + h}\bar{\psi}_i + \frac{h}{2\tau_{\psi} + h}\psi_i^{eq} + \frac{\tau_{\psi} h}{2\tau_{\psi} + h}S_i^{\psi}. \quad (28)$$

Thus, the flux $J^{\psi,n+1/2}$ can be evaluated from Eq. (22). And, finally, $\tilde{\psi}_i^{n+1}$ can be obtained according to Eq. (24) with the two following equations:

$$\bar{\psi}_i^{+} = \frac{2\tau_{\psi} - h}{2\tau_{\psi} + \Delta t}\tilde{\psi}_i + \frac{3h}{2\tau_{\psi} + \Delta t}\psi_i^{eq} + \frac{3\tau_{\psi} h}{2\tau_{\psi} + \Delta t}S_i^{\psi}, \quad (29)$$

$$\tilde{\psi}_i^{+} = \frac{4}{3}\bar{\psi}_i^{+} - \frac{1}{3}\tilde{\psi}_i. \quad (30)$$

The macroscopic variables including order parameter $\phi$, dynamic pressure $p$, and velocity $\boldsymbol{u}$ at each cell center are updated by

$$\phi = \sum_i \tilde{f}_i, \quad (31)$$

$$\boldsymbol{u} = \left(\sum_i \boldsymbol{\xi}_i \tilde{g}_i + \frac{\Delta t}{2}\boldsymbol{F}\right)\Big/\rho, \quad (32)$$

$$p = \frac{RT}{1 - \omega_0}\left[\sum_{i \neq 0} \tilde{g}_i + \frac{\Delta t}{2}\boldsymbol{u} \cdot \nabla\rho + \rho[\Gamma_0(\boldsymbol{u}) - \Gamma_0(0)]\right], \quad (33)$$

where $\tilde{f}_i$ comes from Eq. (23a) with $\psi$ replaced by $f$ and so does $\tilde{g}_i$. The relaxation times are determined by the mobility and kinetic viscosity according to

$$\tau_f = \frac{\mathrm{M}_{\phi}}{RT}, \quad \tau_g = \frac{\mu}{\rho RT}. \quad (34)$$

Generally, two popular approaches are used in the calculation of the dynamic viscosity $\mu$. One approach is the linear interpolation of the reciprocals of the viscosities proposed by Zu and He [51], i.e.,

$$\frac{1}{\mu} = \phi\left(\frac{1}{\mu_H} - \frac{1}{\mu_L}\right) + \frac{1}{\mu_L}. \quad (35)$$

The other common approach is to use a linear interpolation expressed as

$$\mu = \phi(\mu_H - \mu_L) + \mu_L. \tag{36}$$

The reciprocal interpolation scheme shows a better accuracy while a simple interpolation scheme is able to enhance modeling stability. A detailed comparison between these two approaches is presented in Sec. IV B.

Since all of the tests in this paper use a uniform Cartesian grid, a six-point numerical scheme [54] is applied for the computation of $\nabla\phi$, which is the only gradient term that needs to be updated. The Laplace operator is calculated by a general nine-point finite difference scheme to ensure the isotropic property. The temporal derivative in Eq. (16) is calculated by the first-order forward Euler scheme. The time step in this work is determined by the CFL condition, as follows:

$$\Delta t = \alpha \frac{\Delta x}{\sqrt{3RT}}, \tag{37}$$

where $\alpha$ stands for the CFL number and $\Delta x$ measures the size of the cell.

It is worth noting that Zhang and Guo [41] proposed a quasi-incompressible model based on DUGKS. Here, we give some comments on the difference between the model of theirs and ours. First, the governing equations used to capture the interface in Guo's model is the Cahn-Hilliard (CH) equation [55,56] while the Allen-Cahn (AC) equation [42–44] is employed in this model. Wang *et al.* [50] make detailed comparison of the results obtained by solving these two equations with the lattice Boltzmann method. It is found that the Allen-Cahn–based lattice Boltzmann model shows a better performance in accuracy and stability. Second, the mass equations used to describe the flow field are different. In Guo's method, a quasi-incompressible model [48] is adopted, with which the uniform mass conservation can be guaranteed while the divergence-free velocity condition is introduced in this model and mass conservation can only be ensured in the single-phase zone. The phenomenon of mass generation or consumption can be observed in the mixing layer when a density contrast exists, as is explained in the first part of this section. Lastly, the number of first-order and second-order derivative terms that need to be updated during the iterative process is different. For Guo's model, three first-order derivative terms including $\nabla\rho$, $\nabla p$, $\nabla\mu_\phi$ and two second-order derivative terms covering $\Delta\mu_\phi$ and $\Delta\phi$ need to be calculated during each iterative process due to the introduction of the quasi-incompressible model. Since the calculation of a $\mu_\phi$ has already involved a second-order derivative term, a fourth-order derivative term needs to be calculated to obtain an accurate $\Delta\mu_\phi$, actually. Those miscellaneous but indispensable derivatives may be responsible for the relatively low density ratio (no larger than 10) in each of their tests. In terms of the present method, only two derivative terms, $\nabla\phi$ and $\Delta\phi$, are necessary during the process of calculation. The maximum density ratio can reach as high as 1000 in either static or dynamic cases. In brief, Guo's method gives a more accurate description about mass transfer during the process of phase transition at the price of introducing more spatial derivative terms up to the fourth order and is incapable of dealing with high-density-ratio scenarios. The present method offers a more efficient and concise way in interface capturing and behaves well at a relatively high-density-ratio case except that mass conservation cannot be guaranteed in the mixing zone of a two-phase flow, which is a common problem within the framework of the phase-field theory under the assumption of incompressibility condition [47].

## III. INTERFACE-CAPTURING TESTS

In this section, four typical benchmark problems, including interface diagonal translation, Zalesak's disk rotation, interface elongation, and interface deformation, are used to validate the interface-capturing ability of the present scheme. Each of the velocity fields is specified in advance, hence, only Eq. (5) needs to be solved. The dimensionless parameters, Péclet number, and Cahn number, are defined as [46]

$$\mathrm{Pe} = \frac{U_0 L_0}{\mathrm{M}_\phi}, \quad \mathrm{Cn} = \frac{W}{L_0}, \tag{38}$$

where $U_0$ is the reference velocity and $L_0$ is the side length of computational domain. The grid size $\Delta x$ is kept at unity and the CFL number remains at 0.5 unless otherwise specified. To quantitatively evaluate the performance of the present method and make a comparison with the results of the LB method, the $L_2$-norm-based error of the order parameter is used [23]:

$$E_\phi = \frac{\sum_{\boldsymbol{x}} |\phi(\boldsymbol{x}, T) - \phi(\boldsymbol{x}, 0)|^2}{\sum_{\boldsymbol{x}} |\phi(\boldsymbol{x}, 0)|^2}. \tag{39}$$

### A. Interface diagonal translation

A circular interface with radius $R = L_0/4$ is settled at the center of a square domain with $L_0 \times L_0$ cells. Periodic boundary condition is applied to all of its sides. The uniform velocity field is specified as

$$u(x, y) = U_0, \quad v(x, y) = U_0. \tag{40}$$

The circular interface would move back to its initial location after $T = L_0/U_0$ time. A comparison based on the convergence rate between the current scheme and the LB method [52] is provided. The effects of Péclet number and mobility coefficient are also investigated.

To obtain the convergence rate, the grid number along each side of the square is refined from 128 to 512. In order to keep the Péclet number, Cahn number, and mobility coefficient constant, the reference velocity $U_0$ and interface width $W$ are tuned along with the variation of grid number. Comparison results shown in Fig. 1 exhibit a second-order convergence accuracy of both DUGKS and LB method. The overall error yielded by DUGKS is a bit higher than that of the LB method, and for DUGKS has a relatively larger numerical dissipation [31].

The reference velocity is used to tune the Péclet number to investigate its effect on the relative error. The other parameters, including the mobility coefficient, reference length, and Cahn number, are kept at a constant value. When it comes to the effect of mobility coefficient, also the reference velocity is tuned to keep the Péclet number fixed. The reference length keeps a constant value of 256 and the Cahn number is $4/256$. Results pertaining to Pe and $\mathrm{M}_\phi$ are presented in Tables I and II, respectively.

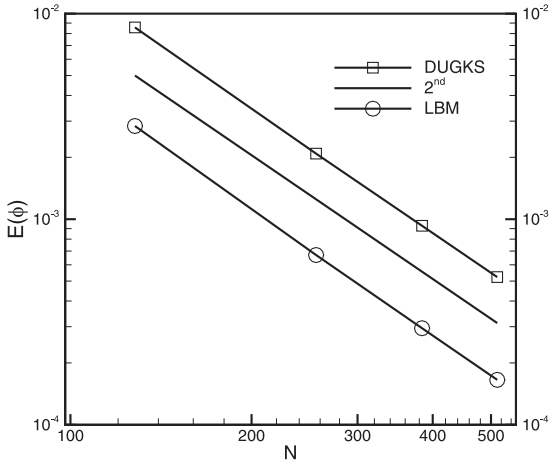


FIG. 1. Convergence rate of DUGKS and LBM, Pe = 128, Cn = 1/32, $M_\phi = 0.02$, $\Delta t = 0.5$.

It can be shown in Table I that the relative error of DUGKS continues increasing as the Péclet number goes up gradually while the results of LBM always remain at the same level. The differences are caused by the reconstruction method adopted in the evaluation of flux. As is mentioned in Sec. II B, a central scheme instead of upwind scheme is used to ensure the low numerical dissipation. Since the Péclet number indicates the ratio of the rate of advection by the rate of mobility driven by a gradient, the flow is mainly dominated by advection when the Péclet number is relatively large. Surely, the central scheme used in flux evaluation would cause deviations under such a circumstance. To overcome this problem, a high-order upwind scheme needs to be developed. Table II gives the relative error of the order parameter for DUGKS and LBM at Pe = 256. Both of these two methods give stable results with an magnitude order as low as $1\times10^{-3}$ despite the increase of mobility.

In a scenario of uniform velocity field, the performance of DUGKS fails to compare with that of the LB method at a relatively large Péclet number, while DUGKS is able to give results comparable to the LB method when the Péclet number is relatively low.

### B. Zalesak's disk rotation

As shown above, the diagonal translation of circular interface does not involve any sharp interface. To further explore the ability of the present method in capturing sharp interface, Zalesak's disk [51,57,58] test is conducted. The disk with a slot is initially located at the center of a 256 × 256 square domain, as illustrated in Fig. 2. The radius of the disk is set as 100 and the width of the slot is 20. The disk is driven by a

TABLE I. $L_2$ error of $\phi$ for interface diagonal translation, $M_\phi = 0.02$, $L_0 = 256$, Cn = 4/256.

| Pe | 128 | 256 | 512 | 1024 |
|---|---|---|---|---|
| DUGKS | $3.6470\times10^{-3}$ | $5.7916\times10^{-3}$ | $1.1548\times10^{-2}$ | $2.3409\times10^{-2}$ |
| LBM | $1.9808\times10^{-3}$ | $1.9769\times10^{-3}$ | $1.9669\times10^{-3}$ | $1.9173\times10^{-3}$ |

TABLE II. $L_2$ error of $\phi$ for interface diagonal translation, Pe = 256, $L_0 = 256$, Cn = 4/256.

| $M_\phi$ | 0.02 | 0.04 | 0.064 | 0.1 |
|---|---|---|---|---|
| DUGKS | $5.7916\times10^{-3}$ | $5.1422\times10^{-3}$ | $5.3437\times10^{-3}$ | $6.4816\times10^{-3}$ |
| LBM | $1.9769\times10^{-3}$ | $1.9720\times10^{-3}$ | $2.0981\times10^{-3}$ | $2.8430\times10^{-3}$ |

irrotational flow field governed by

$$u(x,y) = -\frac{U_0\pi}{L_0}(y - 0.5L_0),$$
$$v(x,y) = \frac{U_0\pi}{L_0}(x - 0.5L_0). \tag{41}$$

In theory, the disk would return to its initial position after $T = 2L_0/U_0$ time. The Cahn number is fixed at 4/256. The order parameter inside the disk is initialized by $\phi_H$ and $\phi_L$ accounts for the rest part. As a diffusive interface method, a transition layer is necessary for the description of the interface. However, no smooth function is available at start time to generate this transition layer in the current case. Thus, there exist discontinuities in the vicinity of the step-shaped interface.

We first make a comparison of the interface patterns obtained respectively with DUGKS and LBM after one cycle, which are shown in Figs. 3–6. Both DUGKS and LBM can give a stable evolution of the interface and no sawtooth phenomenon [23] is observed. At low Péclet numbers (128 and 256), DUGKS is able to capture the interface as accurate as the LBM. As the Péclet number increases, a small amount of distortion at the tip of the slot can be observed, which is mainly caused by the relatively higher numerical dissipation of DUGKS compared to LBM.

To give a quantitative analysis on the results of DUGKS and LBM, the relative error of the order parameter in terms of Péclet number is presented in Table III. It can be found that the results achieved by both methods in the end show a large deviation from the initial distribution of $\phi$. As mentioned

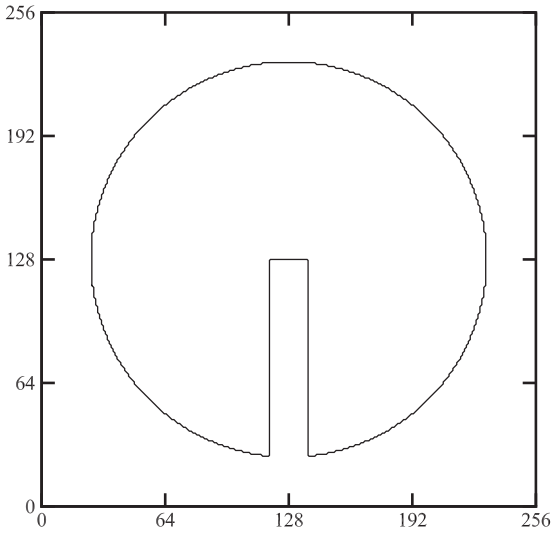


FIG. 2. Initial state of Zalesak's disk, Cn = 4/256, $M_\phi = 0.02$.

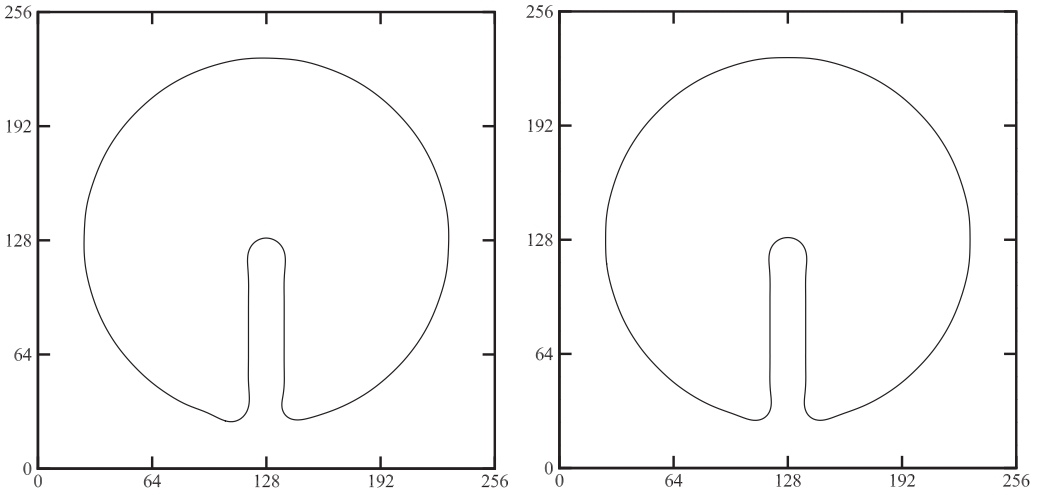


(a)DUGKS (b)LBM

FIG. 3. Results of Zalesak's disk after one period at Pe = 128.

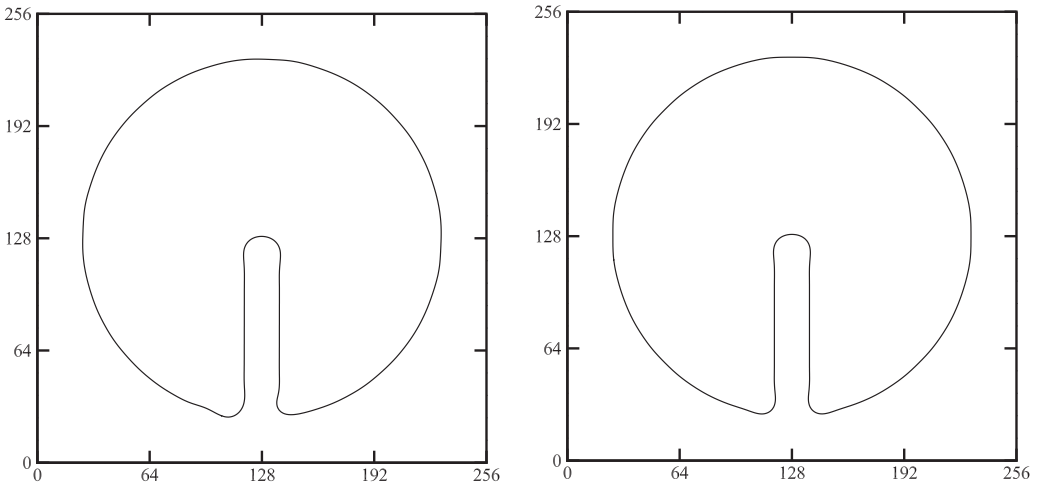


(a)DUGKS (b)LBM

FIG. 4. Results of Zalesak's disk after one period at Pe = 256.

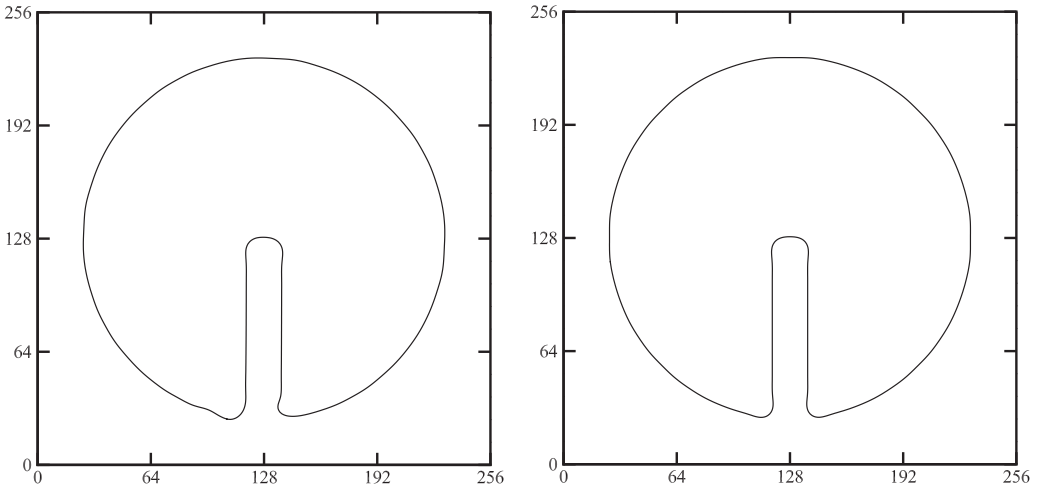


(a)DUGKS (b)LBM

FIG. 5. Results of Zalesak's disk after one period at Pe = 512.

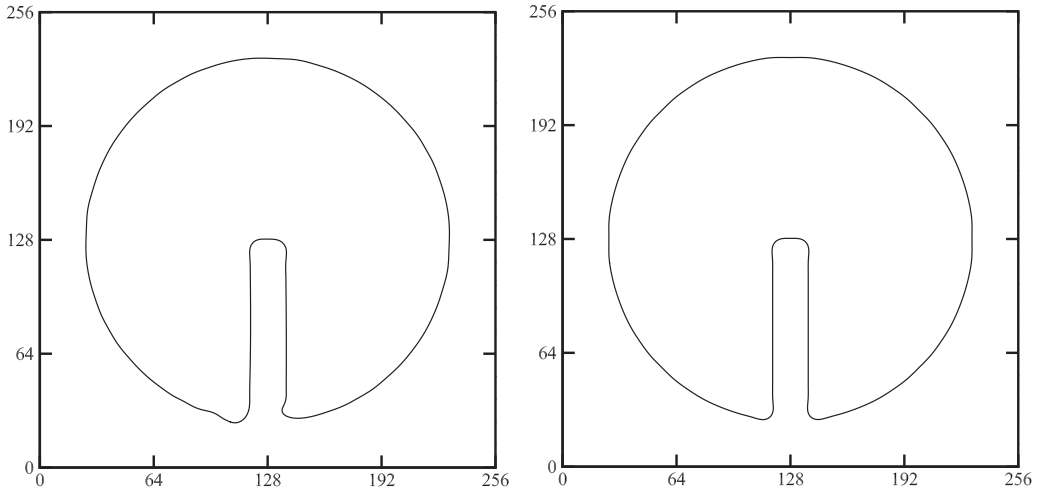


FIG. 6. Results of Zalesak's disk after one period at Pe = 1024.

above, no smooth function is adopted to define the interface. Hence, the interface width is zero at initial time. However, interface with a certain width is formed during the process of evolution. That is why a relatively large deviation between the results achieved at initial and final moment exists. This viewpoint can also explain the same phenomenon shown in Table IV, in which results concerning the effect of mobility coefficient are presented.

### C. Interface elongation in a shear flow

Neither of the above two cases deal with large shape deformation as the interface remains unchanged during the evolution process. To further validate the ability of the present method in capturing interface deformation, the circular interface elongation in a shear flow is studied. In this case, a circular interface with radius $R = L_0/5$ is initially placed at $x = 0.5L_0$ and $y = 0.3L_0$ in a square domain with $L_0 \times L_0$ cells, where $L_0 = 256$ is the reference length. The velocity field is governed by

$$u(x, y) = U_0\pi \sin\left(\frac{\pi x}{L_0}\right)\cos\left(\frac{\pi y}{L_0}\right),$$
$$v(x, y) = -U_0\pi \cos\left(\frac{\pi x}{L_0}\right)\sin\left(\frac{\pi y}{L_0}\right). \quad (42)$$

After $L_0/U_0$ time, the velocity field is reversed to its opposite direction. In this way, the elongated interface would recover to its initial state after another $L_0/U_0$ time. The whole time used in this process is defined as the time period $T = 2L_0/U_0$. The interface is displayed by the contour level of $\phi = 0.5(\phi_H + \phi_L)$. Figures 7–10 illustrate the stretching process of the interface obtained by the present method and LBM. At the time of $t = 0.5T$, the tail tip of the stretched interface is about to break in LBM while DUGKS is able to maintain this tail tip stable. The velocity field is reversed afterward and the stretched interface starts to recover. At $t = 0.75T$, the contour of interface shown in Fig. 9 is approximate to the results presented in Fig. 7 except a small distortion at the tip of stretched interface. After a period time, the stretched interface is restored back up to its original shape, which is shown in Fig. 10. A close inspection toward the results in Fig. 10 shows that there exists a slight deviation at the lower-left part of the interface between the final (solid line) and initial (dashed dotted line) moments, which originates from the tip distortion during the process of restoration. To give a quantitative description about this deviation, the relative error of order parameter in terms of the Péclet number is calculated and presented in Table V. As the Péclet number increases, a tiny increment can be observed in the relative error obtained with DUGKS while results achieved with LBM remain stable. It is worth noting that at a relatively large Péclet number, DUGKS fails to give a result comparable to that of LBM in the case of interface diagonal translation. In the current test, however, the results obtained by DUGKS and LBM at a large Péclet number are pretty close. The effect of mobility coefficient is also studied and results are presented in Table VI. A same growth trend can be observed in the relative errors obtained with both DUGKS and LBM as the mobility coefficient increases. Also, results produced by DUGKS are comparable with those of LBM at various mobility coefficients.

TABLE III. $L_2$ error of $\phi$ for Zalesak's disk rotation, $M_\phi = 0.02$, $L_0 = 256$, Cn = 4/256.

| Pe | 128 | 256 | 512 | 640 | 1024 |
|---|---|---|---|---|---|
| DUGKS | $1.085\times10^{-1}$ | $1.071\times10^{-1}$ | $1.078\times10^{-1}$ | $1.089\times10^{-1}$ | $1.118\times10^{-1}$ |
| LBM | $1.069\times10^{-1}$ | $1.057\times10^{-1}$ | $1.048\times10^{-1}$ | $1.044\times10^{-1}$ | $1.041\times10^{-1}$ |

TABLE IV. $L_2$ error of $\phi$ for Zalesak's disk rotation, Pe = 256, $L_0 = 256$, Cn = 4/256.

| $M_\phi$ | 0.02 | 0.04 | 0.064 | 0.08 | 0.1 |
|---|---|---|---|---|---|
| DUGKS | $1.071\times10^{-1}$ | $1.068\times10^{-1}$ | $1.065\times10^{-1}$ | $1.068\times10^{-1}$ | $1.070\times10^{-1}$ |
| LBM | $1.057\times10^{-1}$ | $1.048\times10^{-1}$ | $1.058\times10^{-1}$ | $1.059\times10^{-1}$ | $1.061\times10^{-1}$ |

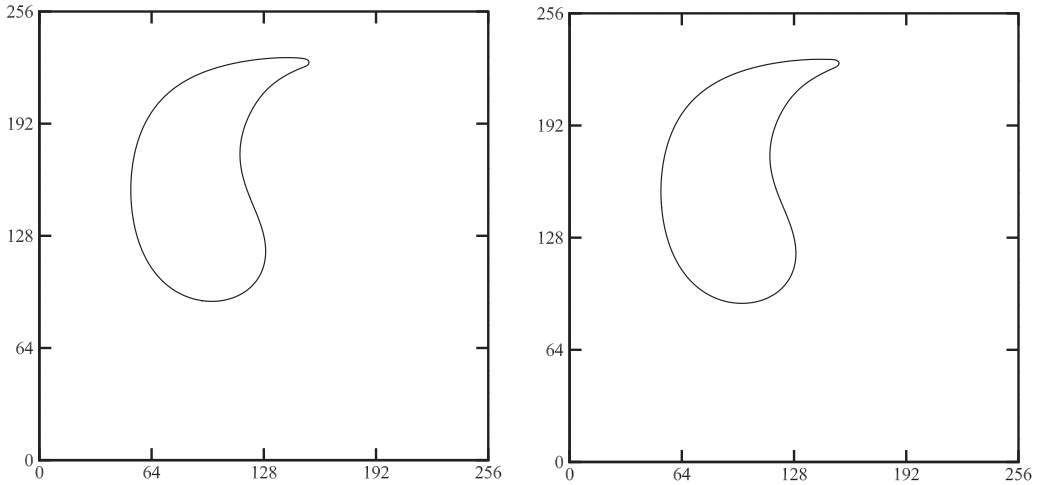


FIG. 7. Results of interface elongation in a shear flow at $t = 0.25T$, $M_\phi = 0.01$, $Pe = 256$.

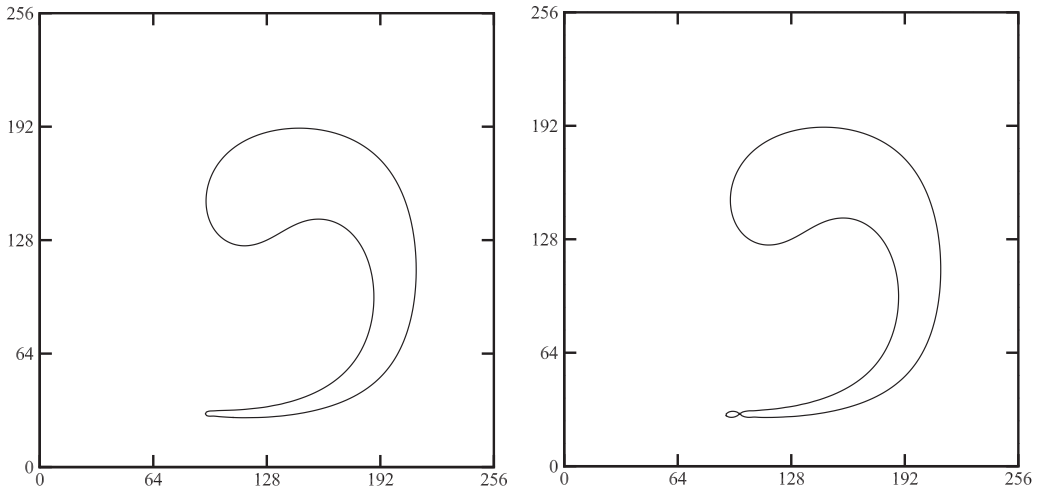


FIG. 8. Results of interface elongation in a shear flow at $t = 0.5T$, $M_\phi = 0.01$, $Pe = 256$.

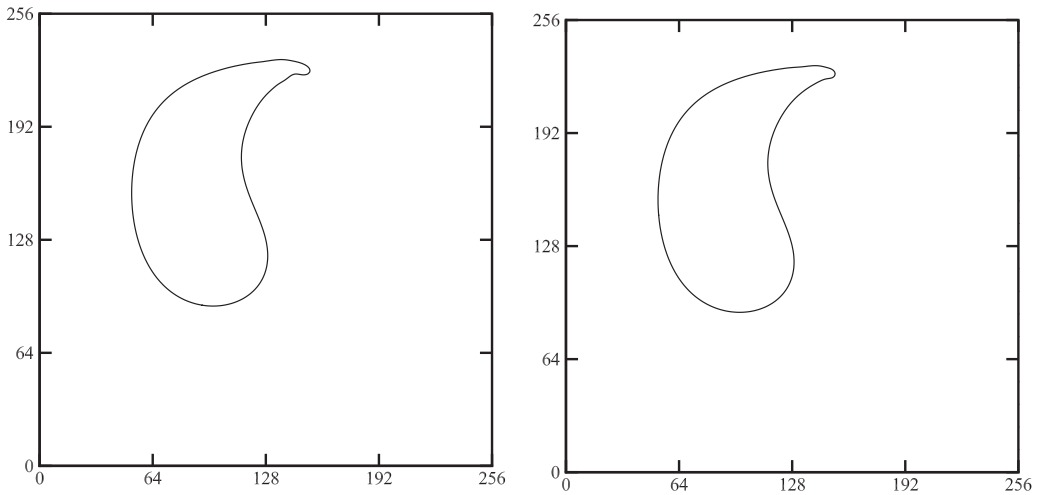


FIG. 9. Results of interface elongation in a shear flow at $t = 0.75T$, $M_\phi = 0.01$, $Pe = 256$.

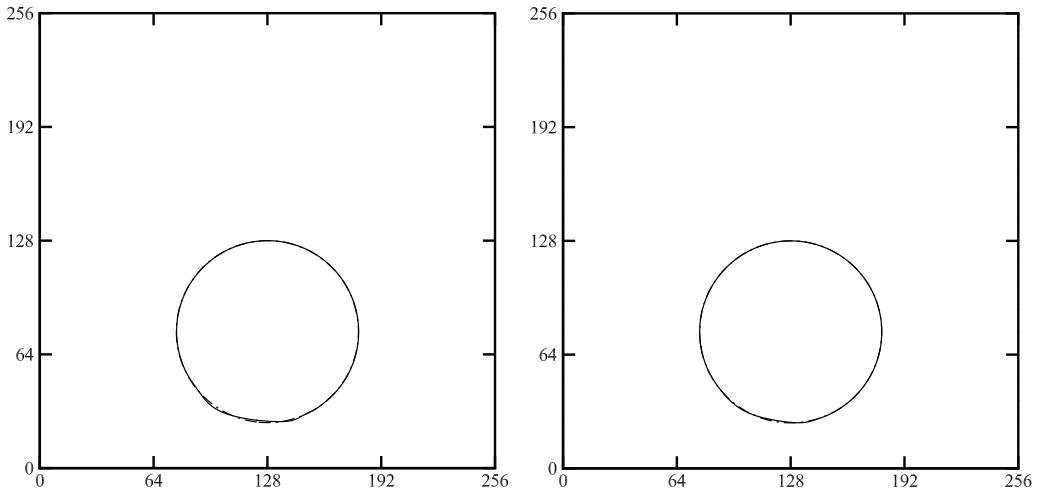


FIG. 10. Results of interface elongation in a shear flow at $t = T$, $M_\phi = 0.01$, Pe = 256.

A further study on the capacity of the kinetic model based on Allen-Cahn equation is conducted with a time-dependent velocity field, which is governed by the same equations used in Liang *et al.* [23]. With such a velocity field, the interface will expose to severe stretch and transform into a long and thin shape. To eliminate the influence caused by numerical schemes, an Allen-Cahn–based multirelaxation-time (MRT) lattice Boltzmann model proposed by Ren *et al.* [46] is used here. The free relaxation parameters except those related to $M_\phi$ are kept at unity. Results at the moment of half-period are shown in Fig. 11. It can be seen clearly that the tail tip of the interface breaks up into small drops. As illustrated by Liang [23], the kinetic model based on Cahn-Hilliard equation is able to capture the long thin tail and the initial circular shape of the interface can be recovered accurately. The deficiency in the Allen-Cahn–based kinetic model may have an impact on numerical simulations referring to subtle interface changes.

### D. Interface deformation in a smoothed shear flow

To further explore the ability of the present method in capturing interface deformation, we continue to conduct another test about the deformation of a circular interface in a smoothed shear flow, which is regarded as one of the most rigorous problems as the interface undergoes a severe deformation [23,44]. The circular interface with a radius $R = L_0/5$ is located at the center of a periodic domain with $L_0 \times L_0$ cells, where $L_0 = 512$ is the reference length. The velocity field is controlled by

$$u(x, y) = -U_0 \sin\left(\frac{4\pi x}{L_0}\right)\sin\left(\frac{4\pi y}{L_0}\right)\cos\left(\frac{\pi t}{T}\right),$$
$$v(x, y) = -U_0 \cos\left(\frac{4\pi x}{L_0}\right)\cos\left(\frac{4\pi y}{L_0}\right)\cos\left(\frac{\pi t}{T}\right), \quad (43)$$

where $U_0$ is the reference velocity and $T = L_0/U_0$ is the period. In the case above, the interface undergoes transfiguration in the first half-period and reconsolidation in the last half-period. The main difference is that a temporal smoothing term $\cos(\frac{\pi t}{T})$ is introduced in the current case to avoid the rapid shift of velocity field. The deformation of the interface driven by a smooth velocity field is shown in Figs. 12–15. It can be found that the results obtained with DUGKS share the same deformation pattern as those of LBM. The restored interface (solid line) after one period time overlaps with the initial one (dashed dotted line) exactly for both methods. In addition, quantitative comparisons between DUGKS and LBM are presented in Tables VII and VIII, illustrating the effects of the Péclet number and mobility coefficient, respectively. It can be shown clearly that even at a large Péclet number, the results provided by DUGKS are almost the same as that of LBM, which is mainly attributed to the finer mesh resolution. As the mobility coefficient increases, DUGKS even shows a better performance than that of the LB method.

From the above cases, we notice that the model based on DUGKS is able to track various deformed interfaces as accurate as LBM when a nonlinear velocity field is imposed, which testify to the capability of DUGKS in interface-tracking simulations.

TABLE V. $L_2$ error of $\phi$ for interface stretch in a shear flow, $M_\phi = 0.01$, $L_0 = 256$, Cn = 4/256.

| Pe | 256 | 512 | 1024 | 1638 |
|---|---|---|---|---|
| DUGKS | $2.596\times10^{-2}$ | $2.831\times10^{-2}$ | $3.246\times10^{-2}$ | $3.798\times10^{-2}$ |
| LBM | $1.405\times10^{-2}$ | $1.232\times10^{-2}$ | $1.309\times10^{-2}$ | $1.653\times10^{-2}$ |

TABLE VI. $L_2$ error of $\phi$ for interface stretch in a shear flow, Pe = 256, $L_0 = 256$, Cn = 4/256.

| $M_\phi$ | 0.01 | 0.02 | 0.04 | 0.05 | 0.064 |
|---|---|---|---|---|---|
| DUGKS | $2.596\times10^{-2}$ | $2.681\times10^{-2}$ | $2.749\times10^{-2}$ | $2.868\times10^{-2}$ | $3.072\times10^{-2}$ |
| LBM | $1.405\times10^{-2}$ | $1.480\times10^{-2}$ | $1.561\times10^{-2}$ | $1.635\times10^{-2}$ | $1.796\times10^{-2}$ |

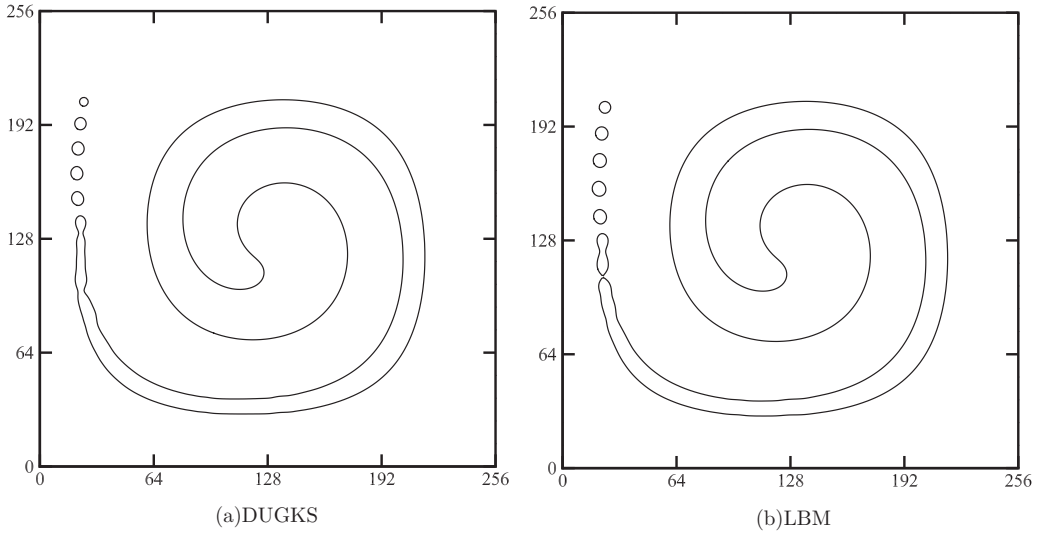


FIG. 11. Results of interface elongation in a shear flow at $t = 0.5T$, $M_\phi = 0.1$, Pe $= 256$.

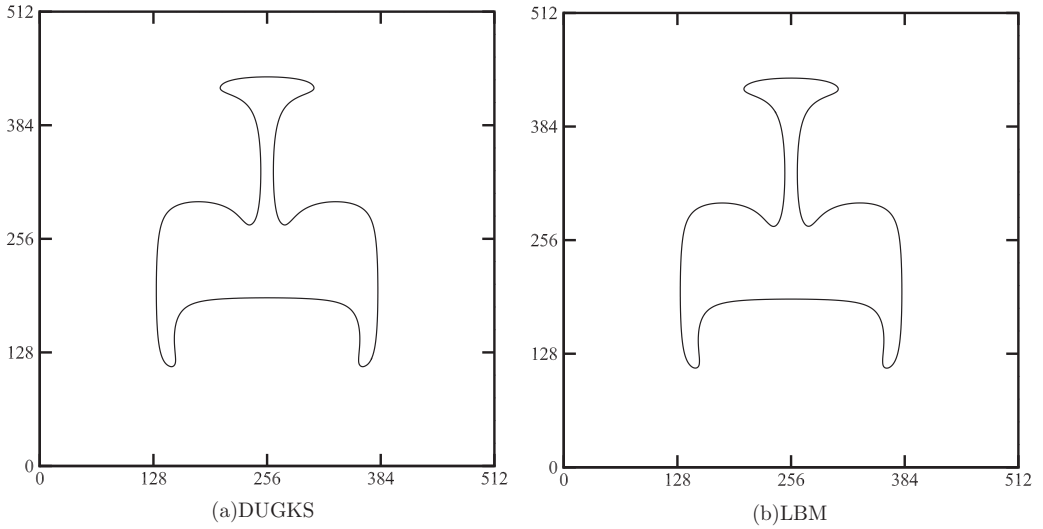


FIG. 12. Results of interface deformation in a smoothed flow at $t = 0.25T$, $M_\phi = 0.02$, Pe $= 2048$.

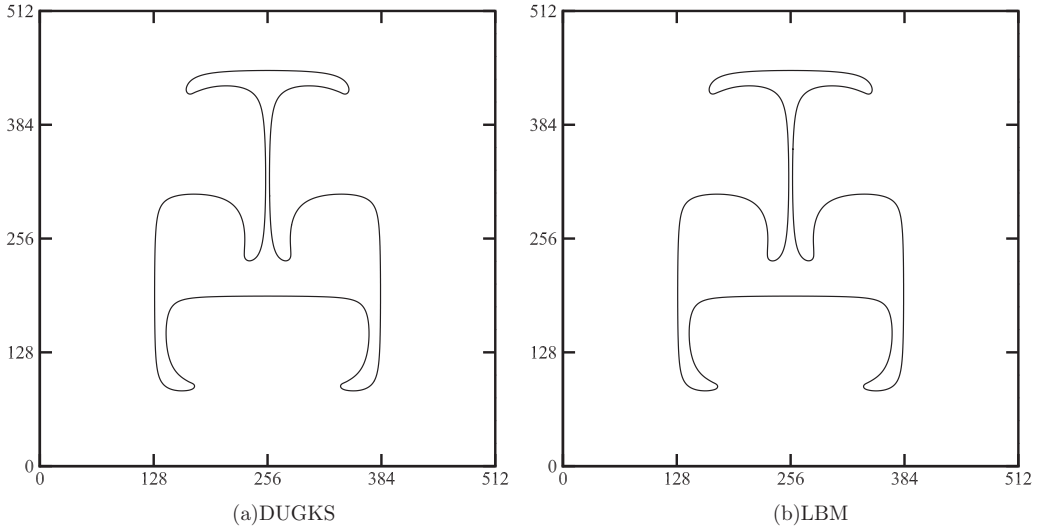


FIG. 13. Results of interface deformation in a smoothed flow at $t = 0.5T$, $M_\phi = 0.02$, Pe $= 2048$.

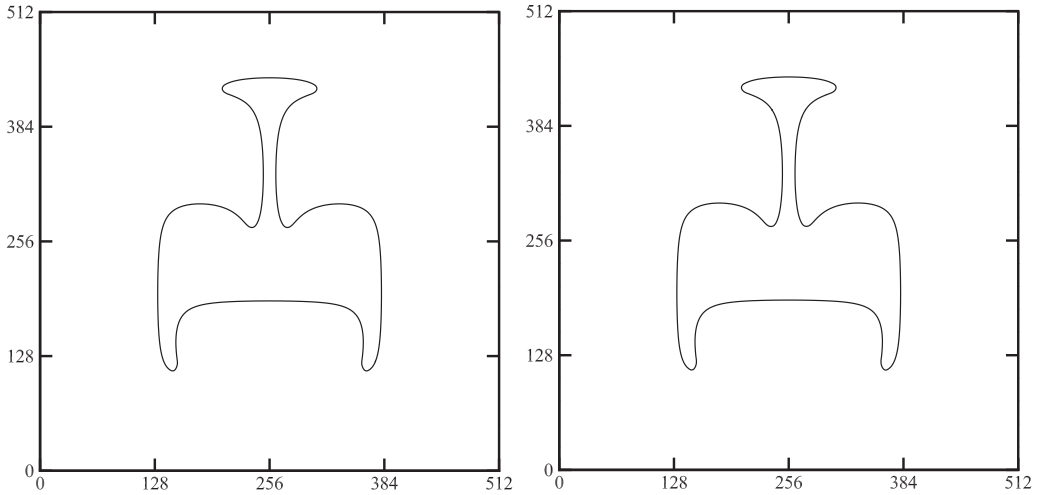


FIG. 14. Results of interface deformation in a smoothed flow at $t = 0.75T$, $M_\phi = 0.02$, Pe = 2048.

## IV. BINARY FLOW TESTS

As the ability of DUGKS in interface capturing has been validated, more tests related to hydrodynamic behavior are used to explore the capacity of the present method. In this section, four benchmark cases including stationary bubble, layered Poiseuille flow, spinodal decomposition, and Rayleigh-Taylor instability are chosen to test and verify the performance of the current model. The convergence criterion for steady flows depends on

$$\frac{\sum_{\boldsymbol{x}} |Q(\boldsymbol{x}, n+1000) - Q(\boldsymbol{x}, n)|^2}{\sum_{\boldsymbol{x}} |Q(\boldsymbol{x}, n+1000)|^2} < 1.0 \times 10^{-8}, \quad (44)$$

where $Q$ stands for either the order parameter $\phi$ or the flow velocity $\boldsymbol{u}$ and $n$ is the time step. The CFL number remains at 0.5 if not otherwise specified.

### A. Stationary bubble

The stationary bubble is a basic problem in verifying newly developed numerical methods [59,60]. At initial state, a light bubble immersed in the heavy liquid is placed at the center of a square domain with $L_0 \times L_0$ cells. Periodic boundary condition is applied to all boundaries. The initial profile of order parameter is given by

$$\phi = \frac{\phi_H + \phi_L}{2} + \frac{\phi_H - \phi_L}{2} \times \tanh\frac{2[\sqrt{(x-x_c)^2 + (y-y_c)^2} - R]}{W}, \quad (45)$$

where $(x_c, y_c)$ is the center of the computational domain and $R$ is the bubble radius. The interface width $W$ is fixed at 5 and the kinetic viscosity $\nu$ remains at 0.1 for the whole flow field. The density ratio varies from 10 to 1000 for different cases. The end condition is determined by Eq. (44) with $Q$ replaced by $\phi$.

The performance of the present method is first examined by Laplace's law. The relationship between pressure difference across the interface and reciprocal of bubble radius is determined by $\Delta P = \sigma/R$, where $P$ is the thermodynamic pressure and is calculated through $P = p_0 - \kappa\phi\Delta\phi + \kappa|\nabla\phi|^2/2 + p$ with the equation of state $p_0 = \phi\partial_\phi\epsilon(\phi) - \epsilon(\phi)$ [23,41,48,61]. Figure 16 presents the validation of Laplace's law based on the current method at a density ratio of 1000. As the surface tension coefficient (STC) increases, obvious deviations between the numerical results (solid line) and analytical results (dashed line with symbols) can be observed. For all situations, the ratio of numerical STC to analytical ones is around 96.5%, which is approximated to the results of Liang *et al.* [23] obtained with an MRT model. The absolute error between the numerical results and analytical results is enlarged with the growth of STC.

Figure 17 depicts the density profile along the vertical center line with various values of mobility coefficient. It can be seen that numerical results match with the analytical solution exactly, which indicates the fundamental ability of the current method in simulation of hydrodynamic problems.

The magnitude of spurious velocity draws attention to numbers of researchers focusing on two-phase problems [62–64]. Here, we give a detailed study on the relationship

TABLE VII. $L_2$ error of $\phi$ for interface deformation in a smoothed flow, $M_\phi = 0.02$, $L_0 = 512$, Cn = 4/512.

| Pe | 512 | 1024 | 1638 | 2048 |
|---|---|---|---|---|
| DUGKS | $9.762\times10^{-3}$ | $7.986\times10^{-3}$ | $1.033\times10^{-2}$ | $1.339\times10^{-2}$ |
| LBM | $9.409\times10^{-3}$ | $7.281\times10^{-3}$ | $9.026\times10^{-3}$ | $1.203\times10^{-2}$ |

TABLE VIII. $L_2$ error of $\phi$ for interface deformation in a smoothed flow, Pe = 512, $L_0 = 512$, Cn = 4/512.

| $M_\phi$ | 0.01 | 0.02 | 0.04 | 0.064 | 0.08 |
|---|---|---|---|---|---|
| DUGKS | $1.051\times10^{-2}$ | $9.762\times10^{-3}$ | $8.652\times10^{-3}$ | $7.880\times10^{-3}$ | $7.570\times10^{-3}$ |
| LBM | $9.422\times10^{-3}$ | $9.409\times10^{-3}$ | $9.355\times10^{-3}$ | $9.255\times10^{-3}$ | $9.178\times10^{-3}$ |

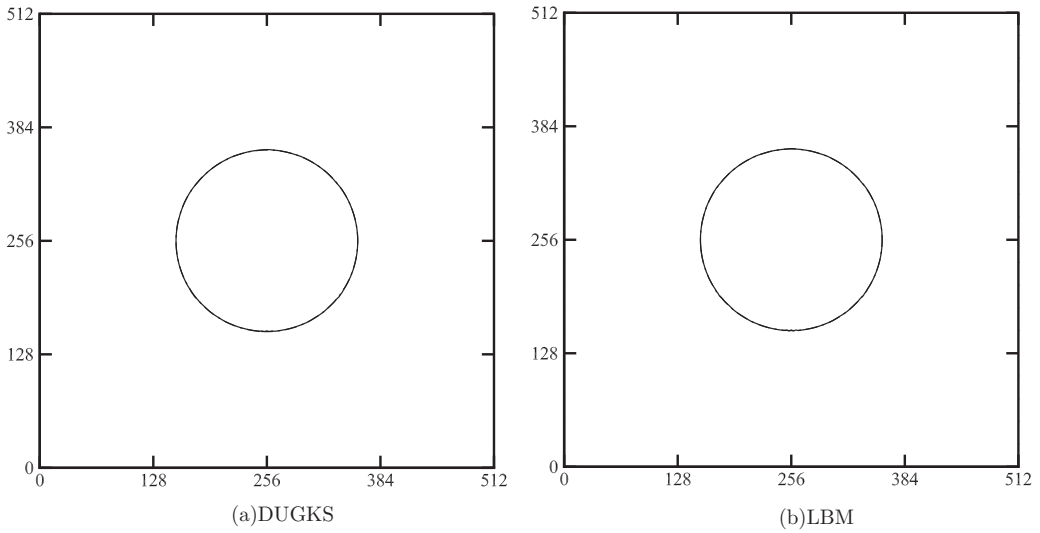


FIG. 15. Results of interface deformation in a smoothed flow at $t = T$, $M_\phi = 0.02$, Pe = 2048.

among density ratio, Laplace number (La), and spurious velocity. The Laplace number is defined as $\sigma\rho_L R/\mu_L^2$, which is different from Liang *et al.* [52]. Figure 18 shows the maximum magnitude of spurious velocity at various La number and density ratio. It can be seen that the maximum magnitude of spurious velocity is linear with La number regardless of the density ratios. Actually, the Laplace number is adjusted with the variation of STC in the current test. Other parameters such as the radius, the density, and dynamic viscosity of light phase are kept at constants. Hence, we can conclude that a linear relationship between the maximum magnitude of spurious velocity and STC is observed. As the density ratio goes up, a significant drop in the maximum magnitude of spurious velocity can be found. The same trend can be observed in Liang's work [52]. The maximum magnitude of spurious velocity is no less than $10^{-6}$ in terms of other previous LB models [23,62,64]. The above results testify that the current method is able to produce lower spurious velocities.

### B. Layered Poiseuille flow

The layered Poiseuille flow is used as a benchmark in the validation of various two-phase approaches [10,46,65]. Two immiscible fluids are driven by a constant body force $\boldsymbol{G} = (G_x, 0)$ in an infinite channel. The upper region of $0 < y \leqslant h$ in the channel is filled with the fluid of small viscosity while the other part is filled with the fluid of large viscosity. Periodic boundary condition is applied to the inlet and outlet and no-slip boundary condition is implemented on the upper and lower walls. When the flow reaches its steady state, the velocity field is consistent with

$$u(y) = \begin{cases} \dfrac{G_x h^2}{2\mu_L}\Big[-\Big(\dfrac{y}{h}\Big)^2 - \dfrac{y}{h}\Big(\dfrac{\mu_L-\mu_H}{\mu_L+\mu_H}\Big) + \dfrac{2\mu_L}{\mu_L+\mu_H}\Big], & 0 < y \leqslant h \\ \dfrac{G_x h^2}{2\mu_H}\Big[-\Big(\dfrac{y}{h}\Big)^2 - \dfrac{y}{h}\Big(\dfrac{\mu_L-\mu_H}{\mu_L+\mu_H}\Big) + \dfrac{2\mu_H}{\mu_L+\mu_H}\Big], & -h \leqslant y \leqslant 0. \end{cases} \tag{46}$$

The central velocity $u_c$ at steady state is related to the constant driving force $G_x$, i.e., $u_c = G_x h^2/(\mu_L + \mu_H)$. The computing process terminates when Eq. (44) is satisfied, with $Q$ replaced by $u$. Two sets of grid, $10\times100$ and $10\times200$, are used in our simulation and comparisons are made between the numerical results and analytical ones. The central velocity $u_c$ is set to be $10^{-4}$, which is small enough to guarantee the incompressible condition. Other parameters are set as $W = 4$, $\sigma = 10^{-3}$, $\rho_H = \rho_L = 1$. Three conditions with different dynamic viscosity ratio are considered in the current case. The results of velocity profile are normalized by the central velocity. Figure 19 presents the velocity profile along the $y$ direction with various viscosity ratios $\mu^*$. It can be found that results obtained with both sets of grid are in good agreement with the analytical solution. The deviation mainly occurs at the interfacial region. As the mesh resolution goes finer, the deviation becomes smaller. A quantitative description of the relative error between the numerical and analytical solutions is presented in Fig. 20. Compared to the results of Ren *et al.* [46], the relative error achieved by DUGKS is a bit larger. This is mainly caused by the different schemes used in the evaluation of dynamic viscosity. To avoid the diffusion effect at the interfacial region, Ren adopts a step function for the dynamic viscosity while a continuous function is implemented in our study. The overall $L_2$-norm error is recorded and it is found that the maximum value of the numerical error is $4.866 \times 10^{-3}$ at the condition of $\mu^* = 1000$, $N_y = 200$, and $1.431 \times 10^{-2}$ at the condition of $\mu^* = 1000$, $N_y = 100$, which have the same order as those in the literature [61]. The results above show that the present method is accurate enough

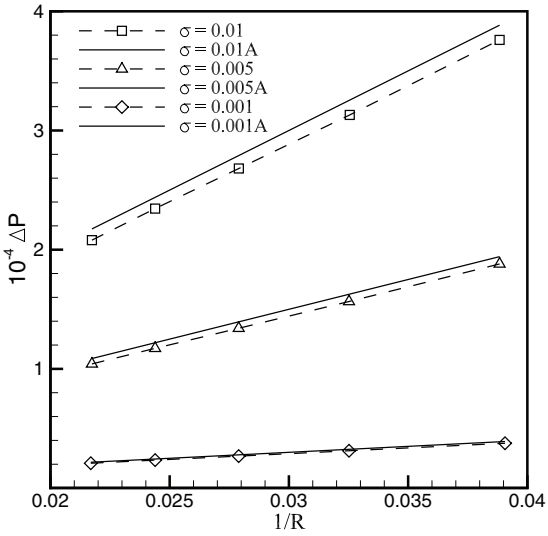


FIG. 16. Validation of Laplace's law with a density ratio of 1000 and $M_\phi = 0.1$.

in simulating two-phase flows involving large viscosity ratio.

In some of others' work [52,66], a linear interpolation of the original dynamic viscosities is used to estimate the viscosity at the interfacial region. Comparisons between the profiles of velocity as well as relaxation time obtained through these two schemes are made and shown in Fig. 21. It can be seen that linear scheme underestimates the velocity profile of large viscosity fluid. As is demonstrated by Zu and He [51], the scheme of inverse linear interpolation ensures the continuity of viscosity flux at the mixture layer. It is reasonable to get a better result using this scheme. Liang *et al.* [65] also adopt the scheme of inverse linear interpolation for the estimation of interfacial viscosity in their new research.

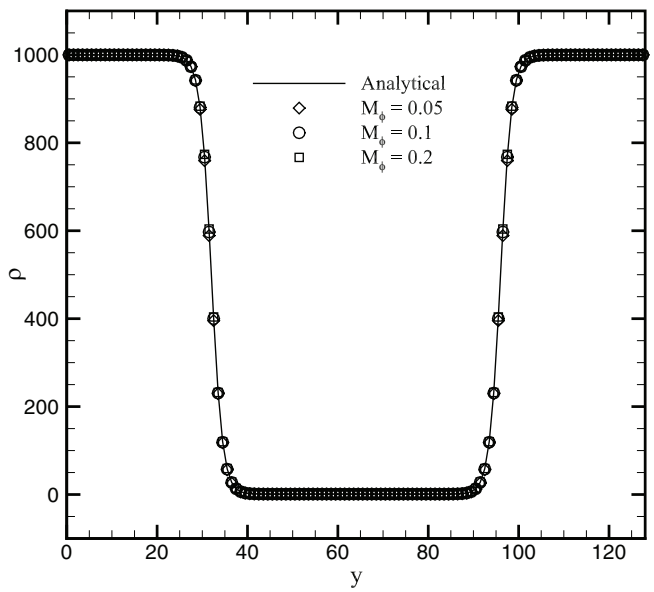


FIG. 17. Density profile along the vertical center line with a density ratio of 1000.

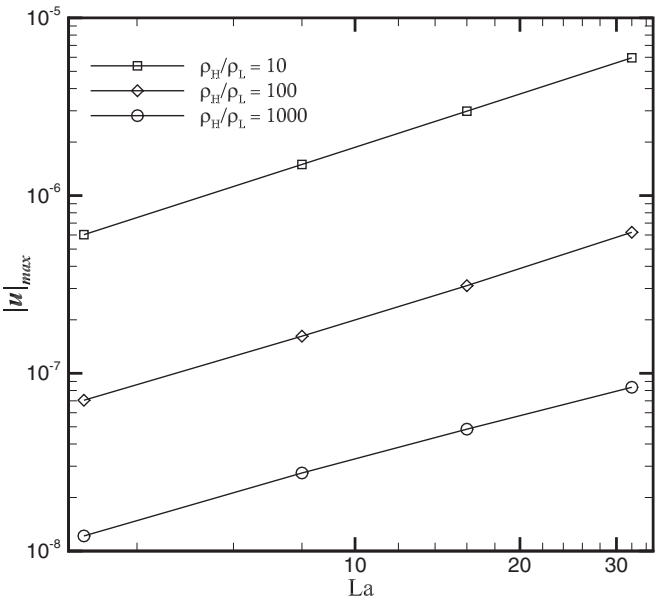


FIG. 18. Maximum magnitude of spurious velocity with various La number and density ratios.

### C. Spinodal decomposition

The spinodal decomposition, also known as phase separation, is a pervasive phenomenon in the study of immiscible fluids. It occurs due to the existence of fluctuations in a homogeneous mixture with a metastable state. Several studies on the spinodal decomposition problem have been carried out with the implementation of LB methods [9,51,52,67]. Among those works, only Liang *et al.* [52] perform a simulation with a large density ratio of 1000. To demonstrate the capability of the current method in the study of phase separation process under large density ratio and to further illustrate the mass diffusion phenomenon during this process, the same spinodal decomposition problem is investigated. Our simulation is carried out in a square domain with a mesh of $200 \times 200$. Periodic boundary condition is implemented at all boundaries. The initial distribution of the order parameter is defined by

$$\phi(x, y) = 0.6 + \text{rand}(x, y), \tag{47}$$

where $\text{rand}(x, y)$ is a random function used to impose fluctuations on the homogeneous mixture. The density field is calculated by Eq. (10), where $\rho_H$ and $\rho_L$ are set to be 1000 and 1, respectively. The kinetic viscosity ratio of $\nu_L$ to $\nu_H$ is fixed at 10. Other parameters are given as $W = 4$, $\sigma = 0.1$, and $M_\phi = 0.1$. The dimensionless evolution time during the phase separation process is defined as $t^* = t/T$, where $T = \rho_H \nu_H W/\sigma$. The termination moment of our simulation is set at $t = 2500$, which is long enough to prove the stability of the current method [51]. Figure 22 depicts several contours of density distribution at various moments extracted from the process of phase separation. At a preliminary state, the small fluctuations in density evolve into large-scale inhomogeneities and interfaces separating different phases are beginning to emerge. Then, the inhomogeneities drive the material of light phase into tiny bubbles with irregular shapes. As the system develops, some of these bubbles keep on coalescing into large

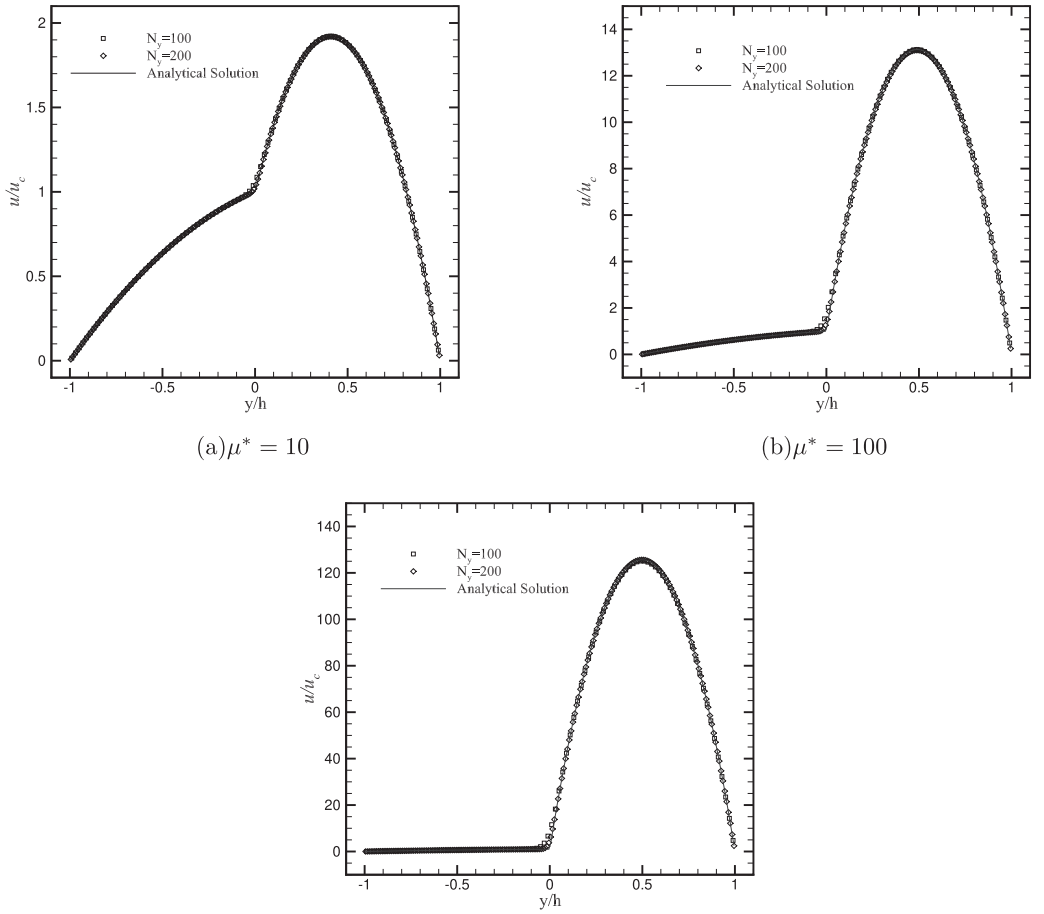


(a)$\mu^* = 10$ (b)$\mu^* = 100$

(c)$\mu^* = 1000$

FIG. 19. Velocity profile of layered Poiseuille flow with various viscosity ratios.

ones. Eventually, a thermodynamic equilibrium state at which binary phases with distinctive contrast can be observed is reached.

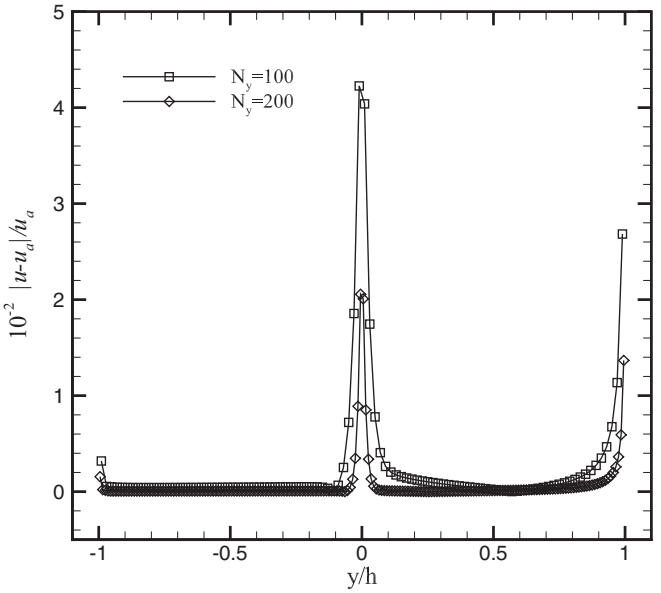


FIG. 20. Relative errors of layered Poiseuille flow with $\mu^* = 10$.

To investigate the conservation of mass, we also record the mass variation in terms of the whole domain during the process of phase separation. Figure 23 illustrates that mass generation and diffusion appears until the system reaches a relatively stable condition where no intensive coalescence or condensation take place. Although the relative value of mass variation is small, it may induce unphysical behaviors at some special conditions [48]. For problems referring to continuous separation of different phases, the quasi-incompressible model in literature [41] should be more reliable.

### D. Rayleigh-Taylor instability

In the final case, the benchmark problem of Rayleigh-Taylor instability (RTI) is conducted. The RTI is a common and important phenomenon in nature, which occurs when a heavy phase is on top of a light phase with initial perturbation in the interface. This benchmark has been extensively studied by several newly developed numerical approaches [10,23,41,47,51,58,61] in order to validate their reliability. The computational domain is a rectangular box with $L_0 \times 4L_0$ cells. The initial interface is located at $H(x, y) = 2L_0 + 0.1L_0\cos(2\pi x/L_0)$ and the initial order profile is defined as

$$\phi(x, y) = \frac{\phi_H + \phi_L}{2} + \frac{\phi_H - \phi_L}{2}\tanh\frac{2[y - H(x, y)]}{W}. \quad (48)$$

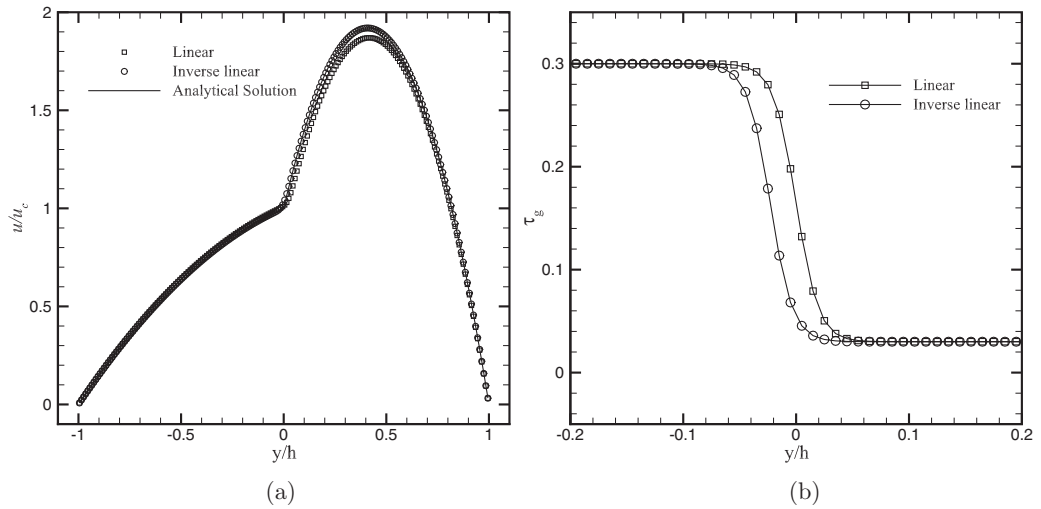


FIG. 21. Velocity profile (a) and relaxation time (b) with different interpolation schemes ($\mu^* = 10$).

Two dimensionless numbers, Atwood number and Reynolds number, are introduced to characterize the RTI problem and their expressions are defined as follows:

$$\mathrm{At} = (\rho_H - \rho_L)/(\rho_H + \rho_L),\ \mathrm{Re} = \rho_H L_0 \sqrt{|G_y L_0|}/\mu, \quad (49)$$

where $G_y$ stands for acceleration of gravity. The relationship of density ratio $\rho^*$ and Atwood number At is $\rho^* = (1 + \mathrm{At})/(1 - \mathrm{At})$. The physical parameters are fixed as $L_0 = 256$, $\sqrt{|G_y L_0|} = 0.04$, $W = 5$, $\sigma = 5\times10^{-5}$ and the reference time is set to be $T = \sqrt{L_0/|G_y \mathrm{At}|}/\Delta t$. The CFL number is adjusted to 0.25 to reduce the temporal dissipation. The no-slip boundary condition is applied to the top and bottom sides and periodic boundary condition is implemented at the left and right sides.

To make a comparison between the results obtained by the current method and other available data presented in literature [41,46,47,58], we first carried out a simulation at the condition of At = 0.5, Re = 3000. Five stages in the evolution of interface are illustrated in Fig. 24. As is observed in previous works, the heavy fluid falls down symmetrically by gravity and the light fluid is driven to rise up on the opposite side. The flow patterns at early stages show the same characteristics as those results presented in literature [46,66] since the elongation of the interface is relatively small. With the evolution of the system, breakups at the rolling-up tail of the interface can be observed clearly. The results obtained with the current method display more severe breakups, which is mainly caused by the larger dissipation feature of DUGKS compared to the LB method. The interface at the top of flow domain is no longer distinguishable when it comes to the end stage of evolution. Actually, if we make a close inspection of the interfacial differences between the results achieved by the Allen-Cahn–based model [46,66] and those from the Cahn-Hilliard–based model [23,47,51] under the framework of the LB method, it can be found that in the results presented by the Allen-Cahn–based model the rolling-up tails of the interface tend to break up at an early stage while an elaborated contour of interface rolling up can be observed and tail breakups are delayed in the results of the Cahn-Hilliard–based model. The rolling up of the interface shown in the current case shares some similarities with the interface elongation problem in Sec. III C. Both of them undergo an interface elongation process during which a smoothed interface is stretched and prolongated. As is depicted in Sec. III, the Cahn-Hilliard–based model shows a better performance than the Allen-Cahn–based model in the interface elongation test. Hence, it is reasonable to get a more distinguishable interface contour with the Cahn-Hilliard–based model. Solving the AC equation in the framework of DUGKS has made its weak points more obvious.

Variations in the dimensionless positions of bubble front of the light phase and spike tip of the heavy phase are shown in Fig. 25. It can be seen that the results presented by the current method are in good agreement with the previous works [41,46,47,58].

To make a further exploration of the capability of the present method, simulations of RTI at two more conditions of At = 0.1, Re = 150 and At = 0.1, Re = 3000 are carried out and the evolution of interface at five different stages is presented in Figs. 26 and 27. At low Reynolds number (Re = 150), there is not much difference between the results of Zhang *et al.* [41] and ours as the interface pattern is simple and no complicated structure is evolved. As the Reynolds number goes higher (Re = 3000), large disparities in the evolution of interface patterns can be observed between these two models. The rolling-up tail of the interface breaks up into small bubbles or drops, which is illustrated by the discrete blue or red spots in Fig. 27 at $t = 2.5T$. With the evolution of the interface, coalescence of these scattered elements can be observed, which means that process of phase separation happens locally. With the development of the system, the tail grows thinner as well as longer. At a certain moment, breakups of this slender tail take place and the interface pattern at $t = 4.0T$ shows up. Compared to the evolution process depicted by Zhang *et al.* [41], the present model fails to give a distinct depiction of interface patterns at a later stage.

To investigate the influence of different hydrodynamic models, another case using the hydrodynamic part of the He-Chen-Zhang (HCZ) model [17] is conducted. Both Fakhari

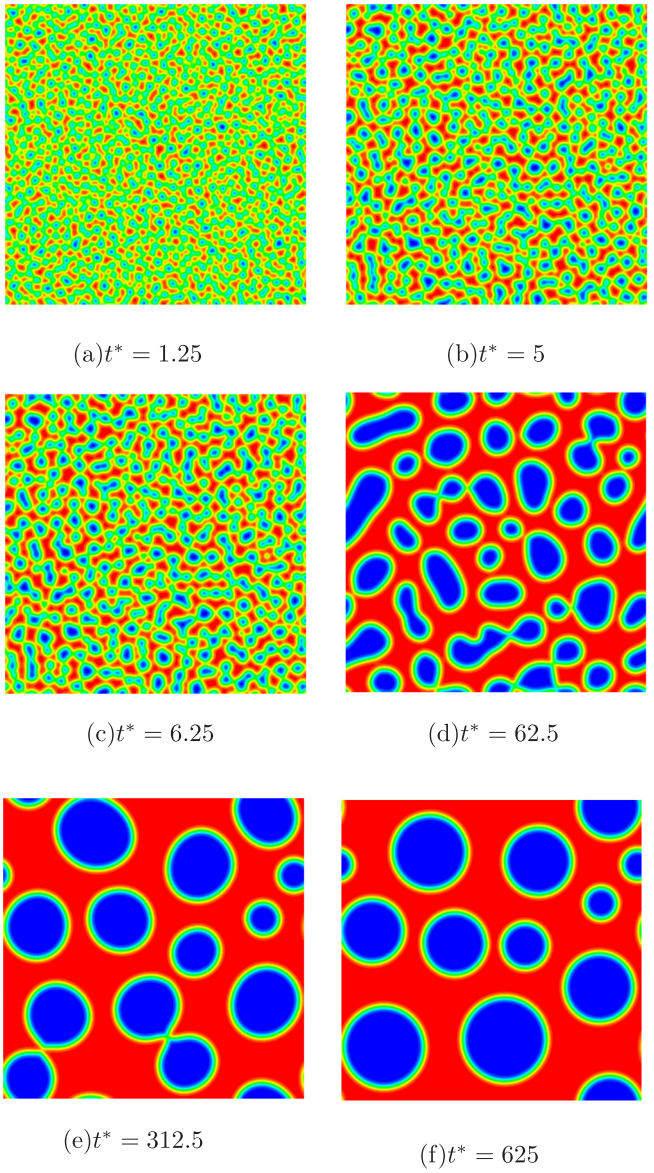


FIG. 22. Contours of density distribution at various moments in the process of phase separation.

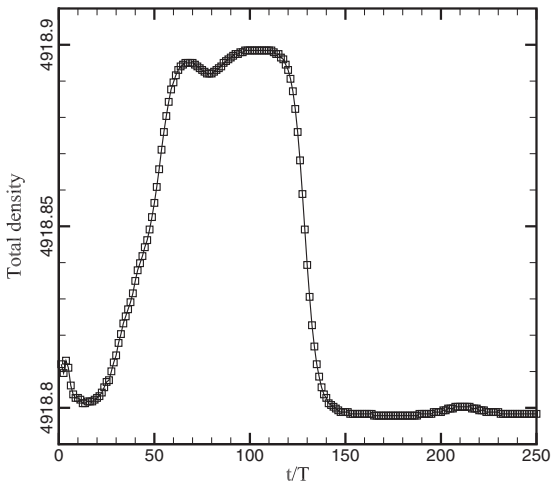


FIG. 23. Mass variation along with the process of phase separation.

*et al.* [68] and Zhang *et al.* [41] adopt this hydrodynamic model to solve the mass and momentum equations. All of the parameters were kept the same as the above one with a condition of At = 0.1, Re = 3000. The time evolution of interface patterns is shown in Fig. 28. At early stages, the interface patterns obtained by two different hydrodynamic models are almost identical. Although slight disparities can be observed at the last two stages, the overall flow patterns obtained by the HCZ model are nearly the same as the results achieved with the hydrodynamic model mainly used in this work. The influence of different hydrodynamic models can be neglected. Hence, the different phase equations should account for the disparities in the evolution of interface patterns discussed above.

With detailed comparisons conducted in this subsection, we can conclude that the failure of DUGKS in the detailed depiction of complex interfaces during the evolution of RTI is to blame for not only the relatively larger dissipation of DUGKS compared to the LB method, but also the weakness of the Allen-Cahn–based models exposed in the scenario of a severely stretched and deformed interface. Since the model based on the LB method shows a better performance than the model based on DUGKS in depicting complex interfaces during the evolution of RTI, it is reasonable to infer that a high-order scheme of DUGKS [69] is able to overcome this problem.

As for the underlying causes of the discrepancy noticed between the Allen-Cahn–based and Cahn-Hilliard–based models, we attempt to explain it from the physical equations employed to implement them. Both the conservative AC equation and CH equation are able to describe phase evolution without an explicit tracking of the interface. The only difference between them is the source term on the right-hand side of the two equations. The source term of the CH equation involves fourth-order partial derivatives, while the source term of the AC equation involves only second-order partial derivatives. The main reason behind the different format in source terms lies in the assumptions. Compared to the derivation of the CH equation [70], a normal interface velocity proportional to the interface curvature is introduced during the derivation of the AC equation [44]. The equilibrium profile of interface also depends on the curvature. The accuracy of curvature plays an important role in interface depiction. When the interface is relatively simple, it is easy to calculate the value of local curvature along with the normal interface velocity accurately. As the interface becomes much more complicated, there may appear precision loss in the computing of local curvature, which in turn leads to the failure in tracking long stretched and severely deformed interfaces. The necessity of accurate curvature value puts a demand on the numerical scheme used to compute it and a high-order numerical scheme is needed in order to track complex interfaces with an Allen-Cahn–based model.

Because the main concern of our study is two-phase flow with a large density ratio, another two cases with larger Atwood number are carried out. Figure 29 shows the time evolution of interface pattern with conditions of At = 0.98 ($\rho^* = 99$), Re = 150 and At = 0.998 ($\rho^* = 999$), Re = 50. Of note

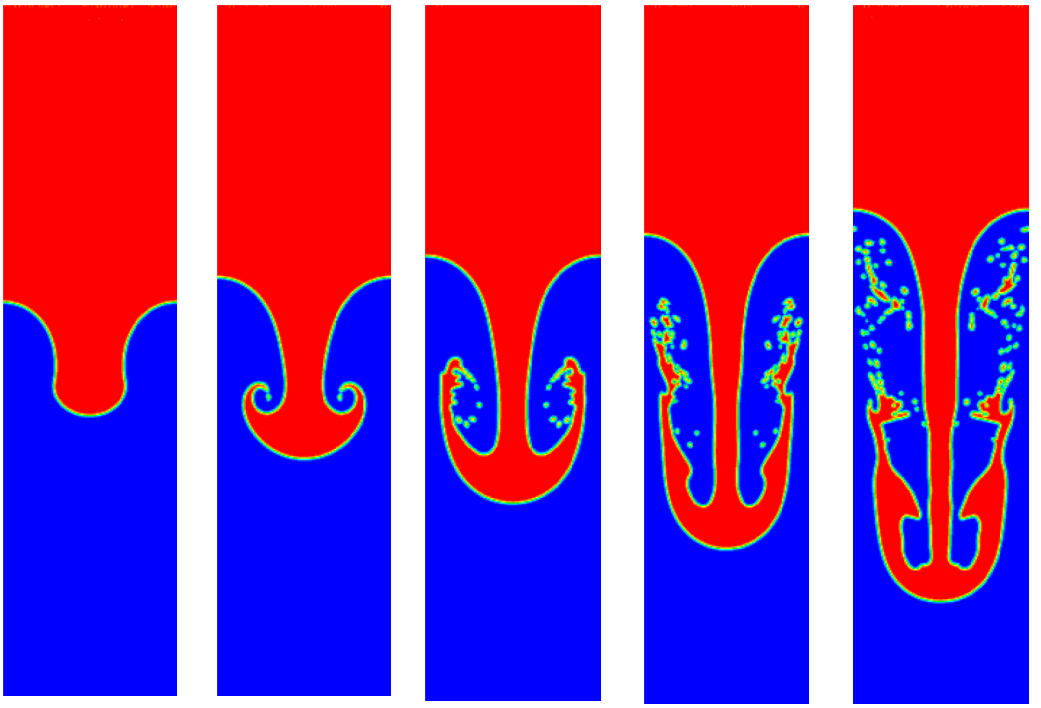

(a)$t = 1.0T$ (b)$t = 1.5T$ (c)$t = 2.0T$ (d)$t = 2.5T$ (e)$t = 3.0T$

FIG. 24. Time evolution of interface patterns of Rayleigh-Taylor instability at At = 0.5 ($\rho^* = 3$), Re = 3000.

is that the interface width $W = 8$ in this simulation. It can be found that the heavy fluid falls directly into the light fluid and no rolling-up behavior of interface is observed. The results obtained here show a considerable similarity with the results of Ren *et al.* [46]. The current method fails to simulate the condition with a higher Reynolds number (At = 0.98, Re = 600), which is mainly caused by the larger dissipation of DUGKS compared to LBM. A high-order scheme is necessary to simulate conditions with high Reynolds number as well as large density ratios [10].

## V. CONCLUSION

In this article, a phase-field method for the simulation of two-phase flows is developed in the framework of DUGKS. The conservative Allen-Cahn equation is used to capture the interface and incompressible hydrodynamic models are employed to solve the velocity and pressure field. The macroscopic equations can be recovered exactly from the discrete kinetic models through the Chapmann-Enskog analysis.

The performance of our proposed model is validated thoroughly by a series of numerical tests. In the interface-

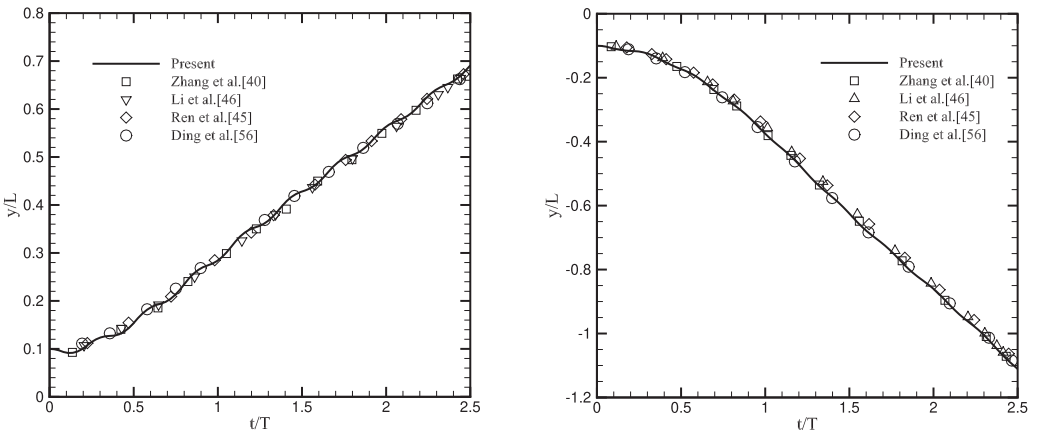


(a)bubble front (b)spike tip

FIG. 25. Time evolution of bubble front and spike tip positions. Comparison with the results of Zhang *et al.* [41], Li *et al.* [47], Ren *et al.* [46], and Ding *et al.* [58].

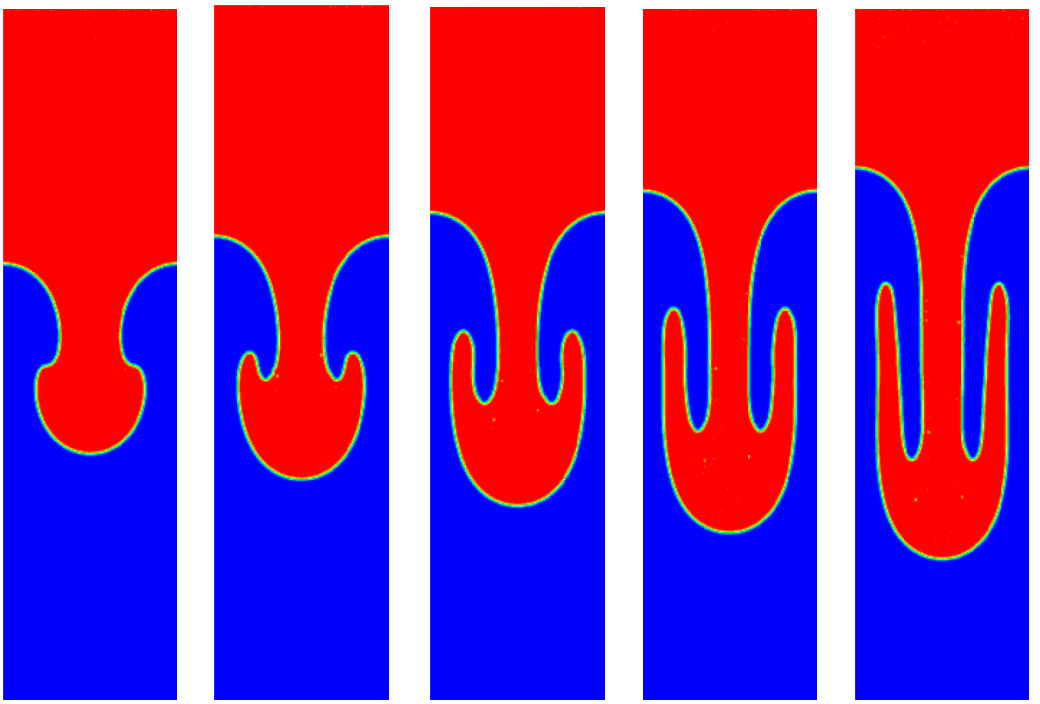

(a)$t = 2.0T$ (b)$t = 2.5T$ (c)$t = 3.0T$ (d)$t = 3.5T$ (e)$t = 4.0T$

FIG. 26. Time evolution of interface patterns of Rayleigh-Taylor instability at At $= 0.1$ ($\rho^* = 1.1/0.9$), Re $= 150$.

capturing tests, our model presents reliable results which are in good agreement with the LB method in terms of the convergence rate and numerical dispersion at various Péclet numbers and mobility coefficients. A key weakness of the Allen-Cahn–based model, ignored by Wang *et al.* [50], is observed in the simulation of interface elongation test. It has been verified that this drawback does have an impact on the results of the Rayleigh-Taylor instability. In the binary flow

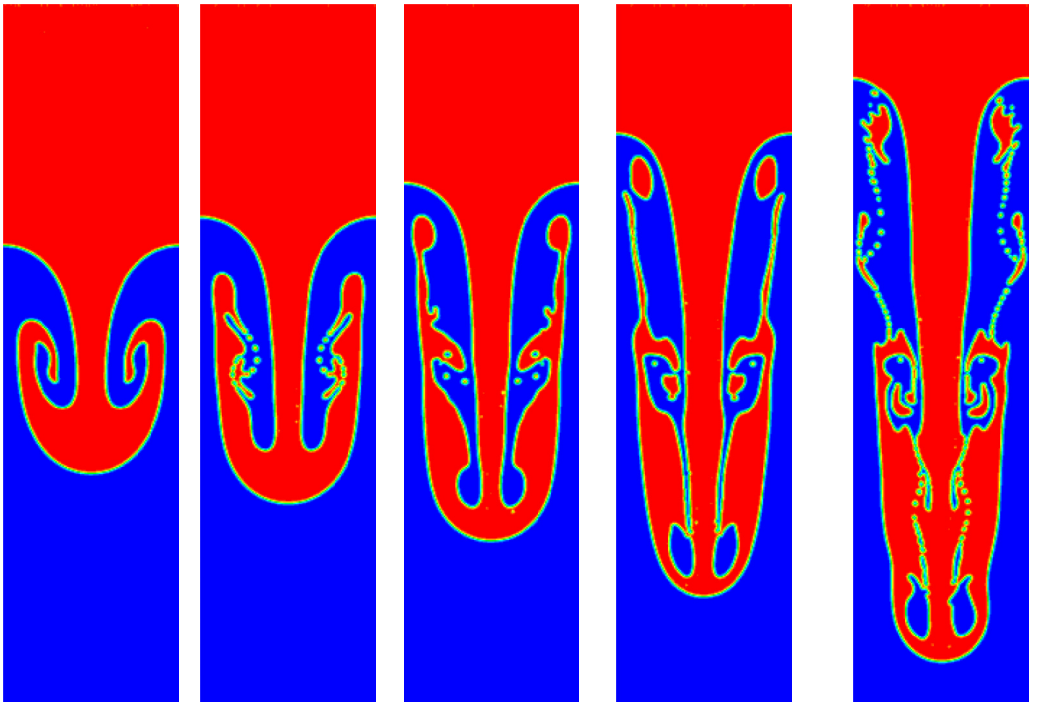

(a)$t = 2.0T$ (b)$t = 2.5T$ (c)$t = 3.0T$ (d)$t = 3.5T$ (e)$t = 4.0T$

FIG. 27. Time evolution of interface patterns of Rayleigh-Taylor instability at At $= 0.1$ ($\rho^* = 1.1/0.9$), Re $= 3000$.

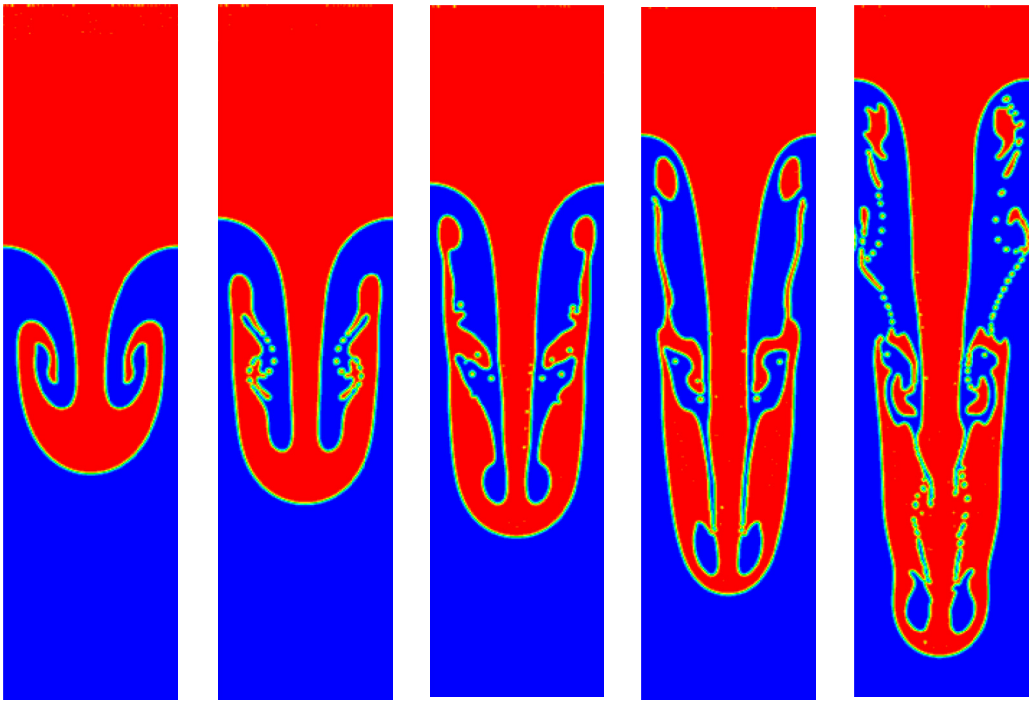

(a)$t = 2.0T$ (b)$t = 2.5T$ (c)$t = 3.0T$ (d)$t = 3.5T$ (e)$t = 4.0T$

FIG. 28. Time evolution of interface patterns of Rayleigh-Taylor instability by the HCZ model at At $= 0.1$ ($\rho^* = 1.1/0.9$), Re $= 3000$.

tests, stationary bubbles with various density ratios are investigated. Laplace's law has been verified and relations between the maximum magnitude of spurious velocity and the Laplace number at various density ratios are disclosed quantitatively. Compared to previous work, a lower magnitude of spurious velocity can be achieved with the present method. In the case of layered Poiseuille flow, the numerical results of velocity profile obtained at high viscosity ratios agree well with the analytical solution. The comparison between two different schemes of viscosity calculation is conducted and similar phenomena to that shown by Zu and He [51] are observed. The capability of the present model in the simulations involving high density ratio is further validated by the spinodal decomposition test. The phenomenon of mass generation or dispersion is observed and the parameter that conservativeness qualifies has been emphasized. The present model fails to give a detailed depiction of the interface patterns in the evolution process of Rayleigh-Taylor instability, which is mainly due to the numerical dissipation of DUGKS. To overcome this problem, a high-order scheme or adaptive mesh refinement technique needs to be implemented.

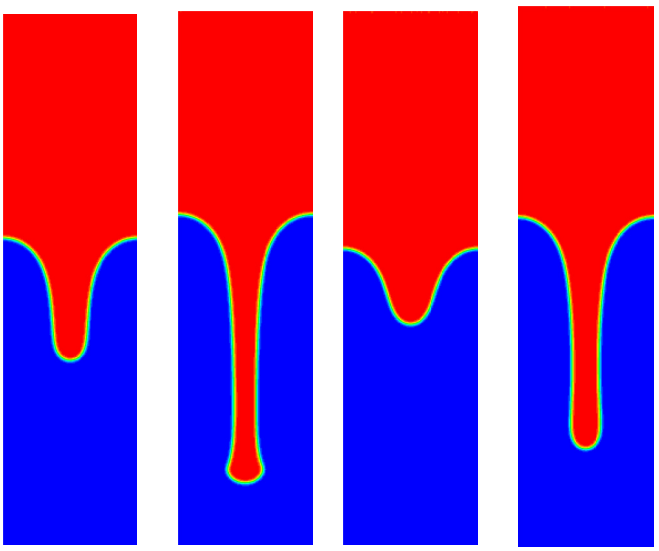

(a)$t = 1.0T$ (a)$t = 2.0T$ (b)$t = 1.0T$ (b)$t = 2.0T$

FIG. 29. Time evolution of interface patterns of Rayleigh-Taylor instability at (a) At $= 0.98$ ($\rho^* = 99$), Re $= 150$; (b) At $= 0.998$ ($\rho^* = 999$), Re $= 50$.

In conclusion, we conduct a preliminary research on the performance of the Allen-Cahn–based two-phase model under the framework of DUGKS. Satisfying results are obtained in several benchmark tests. Compared to the model proposed by Zhang *et al.* [41], a high density ratio of 1000 can be achieved and calculation of source terms referring to high-order derivatives has been simplified. The detailed depiction of the subtle interfaces appeared during the evolution of Rayleigh-Taylor instability is failed. A high-order scheme needs to be developed in future research.

## ACKNOWLEDGMENTS

The project has been financially supported by the National Natural Science Foundation of China (Grant No. 11472219), the 111 Project of China (Grant No. B17037), and the ATCFD Project (No. 2015-F-016).

## APPENDIX: CHAPMAN-ENSKOG ANALYSIS

In this Appendix, the macroscopic equations are recovered from the discrete kinetic equation with the application of Chapman-Enskog analysis. With the introduction of a small parameter $\epsilon$, the discrete distribution function and derivative operators in Eq. (20) can be expanded as

$$\psi_i = \psi_i^{(0)} + \epsilon\psi_i^{(1)} + \epsilon^2\psi_i^{(2)} + \cdots, \tag{A1a}$$

$$\partial_t = \epsilon\partial_{t_0} + \epsilon^2\partial_{t_1}, \quad \nabla = \epsilon\nabla_0, \quad S_i = \epsilon S_i^{(0)}. \tag{A1b}$$

Substituting the above equation into Eq. (20) and rearranging each item based on the power of $\epsilon$, we have

$$\epsilon^0 : \psi_i^{(0)} = \psi_i^{(eq)}, \tag{A2a}$$

$$\epsilon^1 : \partial_{t_0}\psi_i^{(0)} + \boldsymbol{\xi}_i \cdot \nabla_0\psi_i^{(0)} = -\frac{1}{\tau}\psi_i^{(1)} + S_i^{(0)}, \tag{A2b}$$

$$\epsilon^2 : \partial_{t_0}\psi_i^{(1)} + \partial_{t_1}\psi_i^{(0)} + \boldsymbol{\xi}_i \cdot \nabla_0\psi_i^{(1)} = -\frac{1}{\tau}\psi_i^{(2)}. \tag{A2c}$$

First, we give a detailed derivation of the AC equation (5).

The moments of $f_i$ and its corresponding source terms can be calculated by Eqs. (15) and (16), i.e.,

$$\sum_i f_i^{eq} = \phi, \quad \sum_i \boldsymbol{\xi}_i f_i^{eq} = \phi\boldsymbol{u}, \quad \sum_i \boldsymbol{\xi}_i\boldsymbol{\xi}_i f_i^{eq} = \phi RT\boldsymbol{I}, \tag{A3}$$

$$\sum_i F_i^{(0)} = 0, \quad \sum_i \boldsymbol{\xi}_i F_i^{(0)} = \boldsymbol{F}_\phi^{(0)} = \partial_{t_0}(\phi\boldsymbol{u}) + \epsilon\partial_{t_1}(\phi\boldsymbol{u}) + \theta RT\frac{\nabla_0\phi}{|\nabla\phi|}. \tag{A4}$$

Replacing $\psi_i$ with $f_i$ in Eq. (A2) and taking the zeroth- and first-order moments of Eq. (A2b), we have

$$\partial_{t_0}\phi + \nabla_0(\phi\boldsymbol{u}) = 0, \tag{A5a}$$

$$\partial_{t_0}(\phi\boldsymbol{u}) + RT\nabla_0\phi = -\frac{1}{\tau_f}M^{(1)} + \boldsymbol{F}_\phi^{(0)}. \tag{A5b}$$

The zeroth-order moment of Eq. (A2c) is given as

$$\partial_{t_1}\phi + \nabla_0 M^{(1)} = 0. \tag{A6}$$

Calculate $M^{(1)}$ in Eq. (A5b) and substitute it into Eq. (A6), and then we have

$$\partial_{t_1}\phi = \tau_f RT\nabla_0\left(\nabla_0\phi - \theta\frac{\nabla_0\phi}{|\nabla\phi|} - \epsilon\partial_{t_1}(\phi\boldsymbol{u})\right). \tag{A7}$$

Combining Eq. (A7) with Eq. (A5a) and neglecting the term of $O(\epsilon^3)$, the final AC equation (5) can be exactly recovered with $\mathrm{M}_\phi = \tau_f RT$.

Next the recovery of hydrodynamic equations are explained with elaboration. The moments of $g_i$ and its corresponding source terms can be computed from Eqs. (17) and (19), i.e.,

$$\sum_i g_i^{(eq)} = 0, \quad \sum_i \boldsymbol{\xi}_i g_i^{(eq)} = \rho\boldsymbol{u}, \quad \sum_i \boldsymbol{\xi}_i\boldsymbol{\xi}_i g_i^{(eq)} = p\boldsymbol{I} + \rho\boldsymbol{u}\boldsymbol{u},$$

$$\sum_i \boldsymbol{\xi}_i\boldsymbol{\xi}_i\boldsymbol{\xi}_i g_i^{(eq)} = RT\rho\tilde{3}\boldsymbol{u}\boldsymbol{I} = RT\rho(\delta_{\alpha\beta}u_\gamma + \delta_{\beta\gamma}u_\alpha + \delta_{\gamma\alpha}u_\beta), \tag{A8}$$

$$\sum_i G_i = \boldsymbol{u}\cdot\nabla\rho, \quad \sum_i \boldsymbol{\xi}_i G_i = \boldsymbol{F}_s + \boldsymbol{G} = \boldsymbol{F},$$

$$\sum_i \boldsymbol{\xi}_i\boldsymbol{\xi}_i G_i = [\boldsymbol{u}\boldsymbol{F} + \boldsymbol{F}\boldsymbol{u}] + RT[\boldsymbol{u}\nabla\rho + \nabla\rho\boldsymbol{u} + (\boldsymbol{u}\cdot\nabla\rho)\boldsymbol{I}]$$

$$= [u_\alpha F_\beta + u_\beta F_\alpha] + RT[u_\alpha\partial_\beta\rho + u_\beta\partial_\alpha\rho + u_\gamma\partial_\gamma\rho\delta_{\alpha\beta}]. \tag{A9}$$

Since we have the following relations in terms of the conservative variables,

$$\sum_i g_i = 0, \quad \sum_i \boldsymbol{\xi}_i g_i = \rho\boldsymbol{u}. \tag{A10}$$

It is easy to get

$$\sum_i g_i^{(k)} = 0, \quad \sum_i \boldsymbol{\xi}_i g_i^{(k)} = 0, \quad k > 0. \tag{A11}$$

Replacing $\psi_i$ with $g_i$ in Eq. (A2) and taking the zeroth- and first-order moments of Eq. (A2b), we have

$$\nabla \cdot \boldsymbol{u} = 0, \tag{A12a}$$

$$\partial_{t_0}(\rho \boldsymbol{u}) + \nabla_0(\rho \boldsymbol{u}\boldsymbol{u} + p\boldsymbol{I}) = -\frac{1}{\tau_g}\Pi^{(1)} + \boldsymbol{F}^{(0)}, \tag{A12b}$$

where $\Pi^{(1)} = \sum_i \xi_i g_i^{(1)} = 0$.

The zeroth- and first-order moments of Eq. (A2c) are expressed as

$$\nabla_0 \Pi^{(1)} = 0, \tag{A13a}$$

$$\partial_{t_1}(\rho \boldsymbol{u}) = -\nabla_0 \left( \sum_i \boldsymbol{\xi}_i \boldsymbol{\xi}_i g_i^{(1)} \right), \tag{A13b}$$

where

$$\begin{aligned} \sum_i \xi_{i\alpha}\xi_{i\beta} g_i^{(1)} &= -\tau_g \left[ \partial_{t_0}(\rho u_\alpha u_\beta + p\delta_{\alpha\beta}) + RT[\nabla_{0\alpha}(\rho u_\beta) + \nabla_{0\beta}(\rho u_\alpha) + \nabla_{0\gamma}(\rho u_\gamma)] - \sum_i \xi_{i\alpha}\xi_{i\beta} G_i^{(0)} \right] \\ &= -\tau_g RT[\rho \partial_{0\alpha} u_\beta + \rho \partial_{0\beta} u_\alpha] + O(u^3). \end{aligned} \tag{A14}$$

Combining Eq. (A13b) with Eq. (A12b), we get the momentum equation in final form:

$$\partial_t(\rho \boldsymbol{u}) + \nabla \cdot (\rho \boldsymbol{u}\boldsymbol{u} + p\boldsymbol{I}) = \nabla \cdot [\rho \nu (\nabla \boldsymbol{u} + \nabla \boldsymbol{u}^T)] + F, \tag{A15}$$

where $\nu = \tau_g RT$.

Since the computation of dynamic pressure in Eq. (33) is a bit complicated, a detailed derivation is given below. The zeroth-order moment of Eq. (23a) with $\psi_i$ replaced by $g_i$ is given as

$$\sum_i \tilde{g}_i = \frac{2\tau_g + \Delta t}{2\tau_g} \sum_i g_i - \frac{\Delta t}{2\tau_g} \sum_i g_i^{eq} - \frac{\Delta t}{2} \boldsymbol{u} \cdot \nabla \rho, \tag{A16}$$

where $g_i$ can be divided into the equilibrium part $g_i^{eq}$ and nonequilibrium part $g_i^{neq}$. Then, the above equation can be rearranged as

$$\sum_i \tilde{g}_i + \frac{\Delta t}{2} \boldsymbol{u} \cdot \nabla \rho = \sum_i g_i^{eq} + \frac{2\tau_g + \Delta t}{2\tau_g} \sum_i g_i^{neq} = 0. \tag{A17}$$

Subtracting $\tilde{g}_0$ from the left-hand side of the above equation, we get

$$\sum_{i\neq 0} \tilde{g}_i + \frac{\Delta t}{2} \boldsymbol{u} \cdot \nabla \rho = \sum_{i\neq 0} g_i^{eq} + \frac{2\tau_g + \Delta t}{2\tau_g} \sum_{i\neq 0} g_i^{neq} - \underbrace{\frac{\Delta t}{2} G_0}_{O(u^3)}. \tag{A18}$$

With the help of Eq. (A11), the above equation can be rewritten as

$$\sum_{i\neq 0} \tilde{g}_i + \frac{\Delta t}{2} \boldsymbol{u} \cdot \nabla \rho = -g_0^{eq} - \frac{2\tau_g + \Delta t}{2\tau_g} g_0^{neq}. \tag{A19}$$

The nonequilibrium term $g_0^{neq}$ can be dropped since its value is tiny compared to that of $g_0^{eq}$. At last we have

$$\sum_{i\neq 0} \tilde{g}_i + \frac{\Delta t}{2} \boldsymbol{u} \cdot \nabla \rho = -g_0^{eq}. \tag{A20}$$

The dynamic pressure can be finally calculated by Eq. (17).


[1] C. Hirt and B. Nichols, J. Comput. Phys. **39**, 201 (1981).

[2] M. Sussman, P. Smereka, and S. Osher, J. Comput. Phys. **114**, 146 (1994).

[3] S. O. Unverdi and G. Tryggvason, J. Comput. Phys. **100**, 25 (1992).

[4] D. M. Anderson, G. B. McFadden, and A. A. Wheeler, Annu. Rev. Fluid Mech. **30**, 139 (1998).

[5] P. Yue, J. J. Feng, C. Liu, and J. Shen, J. Fluid Mech. **515**, 293 (2004).

[6] R. A. Gingold and J. J. Monaghan, Mon. Not. R. Astron. Soc. **181**, 375 (1977).
[7] L. B. Lucy, Astron. J. **82**, 1013 (1977).
[8] X. He and G. D. Doolen, J. Stat. Phys. **107**, 309 (2002).
[9] Y. Gan, A. Xu, G. Zhang, and S. Succi, Soft Matter **11**, 5336 (2015).
[10] Y. Wang, C. Shu, H. B. Huang, and C. J. Teo, J. Comput. Phys. **280**, 404 (2015).
[11] L. Pan, J. Cheng, S. Wang, and K. Xu, Commun. Comput. Phys. **22**, 1123 (2017).
[12] A. K. Gunstensen, D. H. Rothman, S. Zaleski, and G. Zanetti, Phys. Rev. A **43**, 4320 (1991).
[13] X. Shan and H. Chen, Phys. Rev. E **47**, 1815 (1993).
[14] X. Shan and H. Chen, Phys. Rev. E **49**, 2941 (1994).
[15] M. R. Swift, W. R. Osborn, and J. M. Yeomans, Phys. Rev. Lett. **75**, 830 (1995).
[16] T. Inamuro, T. Ogata, S. Tajima, and N. Konishi, J. Comput. Phys. **198**, 628 (2004).
[17] X. He, S. Chen, and R. Zhang, J. Comput. Phys. **152**, 642 (1999).
[18] H. Liu, L. Wu, Y. Ba, G. Xi, and Y. Zhang, J. Comput. Phys. **327**, 873 (2016).
[19] H. Liu, L. Wu, Y. Ba, and G. Xi, Int. J. Heat Mass Transfer **104**, 337 (2017).
[20] X. Chen, C. Zhong, and X. Yuan, Comput. Math. Appl. **61**, 3577 (2011).
[21] B. Wen, X. Zhou, B. He, C. Zhang, and H. Fang, Phys. Rev. E **95**, 063305 (2017).
[22] J. Y. Shao, C. Shu, H. B. Huang, and Y. T. Chew, Phys. Rev. E **89**, 033309 (2014).
[23] H. Liang, B. C. Shi, Z. L. Guo, and Z. H. Chai, Phys. Rev. E **89**, 053320 (2014).
[24] C. K. Aidun and J. R. Clausen, Annu. Rev. Fluid Mech. **42**, 439 (2010).
[25] Y. Wang, C. Shu, J. Shao, J. Wu, and X. Niu, J. Comput. Phys. **290**, 336 (2015).
[26] G. Gonnella, A. Lamura, and V. Sofonea, Phys. Rev. E **76**, 036703 (2007).
[27] H. Lai, A. Xu, G. Zhang, Y. Gan, Y. Ying, and S. Succi, Phys. Rev. E **94**, 023106 (2016).
[28] C. Lin, A. Xu, G. Zhang, K. H. Luo, and Y. Li, Phys. Rev. E **96**, 053305 (2017).
[29] Z. Guo, K. Xu, and R. Wang, Phys. Rev. E **88**, 033305 (2013).
[30] Z. Guo, R. Wang, and K. Xu, Phys. Rev. E **91**, 033313 (2015).
[31] P. Wang, L. P. Wang, and Z. Guo, Phys. Rev. E **94**, 043304 (2016).
[32] P. Wang, L. Zhu, Z. Guo, and K. Xu, Commun. Comput. Phys. **17**, 657 (2015).
[33] P. Wang, M. T. Ho, L. Wu, Z. Guo, and Y. Zhang, Comput. Fluids **161**, 33 (2018).
[34] C. Wu, B. Shi, Z. Chai, and P. Wang, Comput. Math. Appl. **71**, 2608 (2016).
[35] L. Zhu and Z. Guo, Comput. Fluids (2017), doi: 10.1016/j.compfluid.2017.09.019.
[36] L. Zhu and Z. Guo, Phys. Rev. E **95**, 023113 (2017).
[37] C. Zhang, Z. Guo, and S. Chen, Phys. Rev. E **96**, 063311 (2017).
[38] Y. Zhang, L. Zhu, R. Wang, and Z. Guo, Phys. Rev. E **97**, 053306 (2018).
[39] S. Tao, B. Chen, X. Yang, and S. Huang, Comput. Fluids **165**, 54 (2018).
[40] Y. Huo and Z. Rao, Int. Commun. Heat Mass Transfer **91**, 187 (2018).
[41] C. Zhang, K. Yang, and Z. Guo, Int. J. Heat Mass Transfer **126**, 1326 (2018).
[42] Y. Sun and C. Beckermann, J. Comput. Phys. **220**, 626 (2007).
[43] P. H. Chiu and Y. T. Lin, J. Comput. Phys. **230**, 185 (2011).
[44] M. Geier, A. Fakhari, and T. Lee, Phys. Rev. E **91**, 063309 (2015).
[45] Q. Li, K. H. Luo, Q. J. Kang, Y. L. He, Q. Chen, and Q. Liu, Prog. Energy Combust. Sci. **52**, 62 (2016).
[46] F. Ren, B. Song, M. C. Sukop, and H. Hu, Phys. Rev. E **94**, 023311 (2016).
[47] Q. Li, K. H. Luo, Y. J. Gao, and Y. L. He, Phys. Rev. E **85**, 026704 (2012).
[48] K. Yang and Z. Guo, Phys. Rev. E **93**, 043303 (2016).
[49] Z. Chai, D. Sun, H. Wang, and B. Shi, Int. J. Heat Mass Transfer **122**, 631 (2018).
[50] H. L. Wang, Z. H. Chai, B. C. Shi, and H. Liang, Phys. Rev. E **94**, 033304 (2016).
[51] Y. Q. Zu and S. He, Phys. Rev. E **87**, 043301 (2013).
[52] H. Liang, J. Xu, J. Chen, H. Wang, Z. Chai, and B. Shi, Phys. Rev. E **97**, 033309 (2018).
[53] L. Zhu, P. Wang, and Z. Guo, J. Comput. Phys. **333**, 227 (2017).
[54] C. D. Stiles and Y. Xue, Comput. Fluids **131**, 81 (2016).
[55] J. W. Cahn and J. E. Hilliard, J. Chem. Phys. **28**, 258 (1958).
[56] J. W. Cahn and J. E. Hilliard, J. Chem. Phys. **31**, 688 (1959).
[57] S. T. Zalesak, J. Comput. Phys. **31**, 335 (1979).
[58] H. Ding, P. D. Spelt, and C. Shu, J. Comput. Phys. **226**, 2078 (2007).
[59] A. Fakhari and M. H. Rahimian, Phys. Rev. E **81**, 036707 (2010).
[60] X. Li, D. Gao, B. Hou, and X. Wang, Chem. Eng. Sci. **193**, 76 (2019).
[61] L. Zheng, S. Zheng, and Q. Zhai, Phys. Rev. E **91**, 013309 (2015).
[62] Z. Yu and L. S. Fan, Phys. Rev. E **82**, 046708 (2010).
[63] Z. Guo, C. Zheng, and B. Shi, Phys. Rev. E **83**, 036707 (2011).
[64] Y. Ba, H. Liu, Q. Li, Q. Kang, and J. Sun, Phys. Rev. E **94**, 023310 (2016).
[65] H. Liang, B. Shi, and Z. Chai, Comput. Math. Appl. **73**, 1524 (2017).
[66] A. Fakhari, T. Mitchell, C. Leonardi, and D. Bolster, Phys. Rev. E **96**, 053301 (2017).
[67] A. Xu, G. Gonnella, and A. Lamura, Physica A (Amsterdam) **331**, 10 (2004).
[68] A. Fakhari, M. Geier, and T. Lee, J. Comput. Phys. **315**, 434 (2016).
[69] C. Wu, B. Shi, C. Shu, and Z. Chen, Phys. Rev. E **97**, 023306 (2018).
[70] D. Lee, J. H. Huh, D. Jeong, J. Shin, A. Yun, and J. Kim, Comput. Mater. Sci. **81**, 216 (2014).